Geophysical Journal International

Geophys. J. Int. (2022) **231,** 921–943
Advance Access publication 2022 June 17
GJI Seismology

https://doi.org/10.1093/gji/ggac226

Downloaded from https://academic.oup.com/gji/article/231/2/921/6609778 by OGS (Istituto Nazionale di Oceanografia e di Geofisica Sperimentale-OGS) Borgo Grotta user on 11 December 2023

The AlpArray Research Seismicity-Catalogue

M. Bagagli [1,*] I. Molinari [2] T. Diehl [3] E. Kissling,[1] D. Giardini[1] and the AlpArray Working Group

[1]*Institute of Geophysics, Department of Earth Sciences, ETH, Zürich,* 8006, *Switzerland E-mail: matteo.bagagli@ingv.it*
[2]*Istituto Nazionale di Geofisica e Vulcanologia, Bologna,* 40100, *Italy*
[3]*Swiss Seismological Service, ETH, Zürich,* 8006, *Switzerland*

Accepted 2022 June 15. Received 2021 October 18; in original form 2022 June 9

SUMMARY

We take advantage of the new large AlpArray Seismic Network (AASN) as part of the AlpArray research initiative (www.alparray.ethz.ch), to establish a consistent seismicity-catalogue for the greater Alpine region (GAR) for the time period 2016 January 1–2019 December 31. We use data from 1103 stations including the AASN backbone composed of 352 permanent and 276 (including 30 OBS) temporary broad-band stations (network code Z3). Although characterized by a moderate seismic hazard, the European Alps and surrounding regions have a higher seismic risk due to the higher concentration of values and people. For these reasons, the GAR seismicity is monitored and routinely reported in catalogues by a 11 national and 2 regional seismic observatories. The heterogeneity of these data set limits the possibility of extracting consistent information by simply merging to investigate the GAR's seismicity as a whole. The uniformly spaced and dense AASN provides, for the first time, a unique opportunity to calculate high-precision hypocentre locations and consistent magnitude estimation with uniformity and equal uncertainty across the GAR. We present a new, multistep, semi-automatic method to process ∼50 TB of seismic signals, combining three different software. We used the SeisComP3 for the initial earthquake detection, a newly developed Python library ADAPT for high-quality re-picking, and the well-established VELEST algorithm both for filtering and final location purposes. Moreover, we computed new local magnitudes based on the final high-precision hypocentre locations and re-evaluation of the amplitude observations. The final catalogue contains 3293 seismic events and is complete down to local magnitude 2.4 and regionally consistent with the magnitude 3+ of national catalogues for the same time period. Despite covering only 4 yr of seismicity, our catalogue evidences the main fault systems and orogens' front in the region, that are documented as seismically active by the EPOS-EMSC manually revised regional bulletin for the same time period. Additionally, we jointly inverted for a new regional minimum 1-D *P*-wave velocity model for the GAR and station delays for both permanent station networks and temporary arrays. These results provide the base for a future re-evaluation of the past decades of seismicity, and for the future seismicity, eventually improving seismic-hazard studies in the region. Moreover, we provide a unique, consistent seismic data set fundamental to further investigate this complex and seismically active area. The catalogue, the minimum 1-D *P*-wave velocity model, and station delays associated are openly shared and distributed with a permanent DOI listed in the data availability section.

Key words: Earthquake source observations; Seismicity and tectonics; Statistical seismology.

1 INTRODUCTION

The European Alps and their surrounding mountain ranges (e.g. the northern Apennines, the northwestern Dinarides and the western Carpathians), form a geologically and tectonically complex system of orogens (Fig. 1). This system is composed by continental and

*Now at: Istituto Nazionale di Geofisica e Vulcanologia, ONT, Rome, Italy.

© The Author(s) 2022. Published by Oxford University Press on behalf of The Royal Astronomical Society. This is an Open Access article distributed under the terms of the Creative Commons Attribution License (http://creativecommons.org/licenses/by/4.0/), which permits unrestricted reuse, distribution, and reproduction in any medium, provided the original work is properly cited.

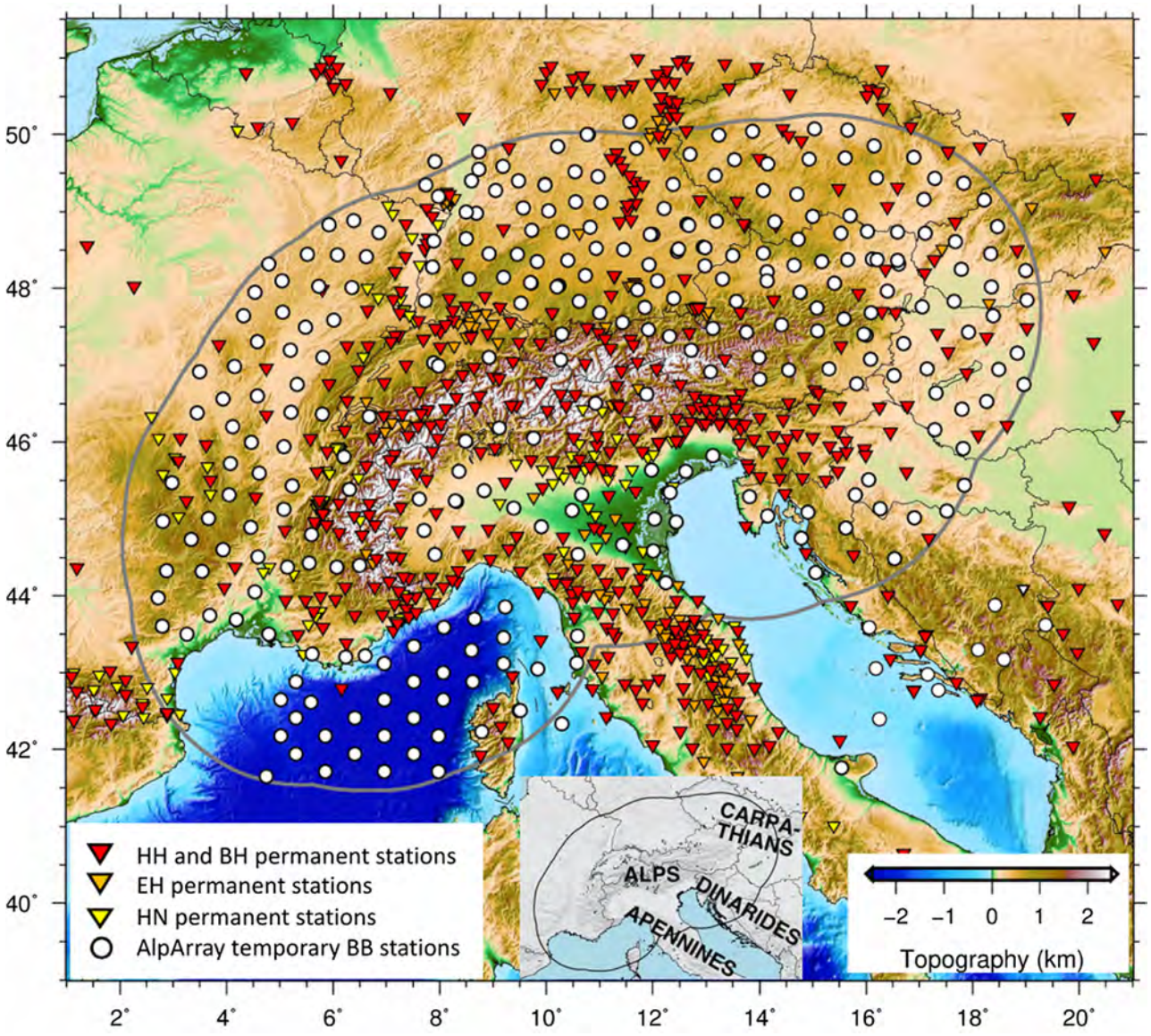

Figure 1. Map of the seismic network used in this study. The light grey contour line delimits the GAR and defines the study area. The GAR is defined by the 250 km distance from the 800 m topography elevation isoline around the Alps. The inset map describes the locations of the four major orogenic belts fully or partly covered by the AASN. The network has a total of 1103 permanent and temporary seismic stations: 849 BB (including 30 OBS, HH-BH), 144 accelerometers (HN) and 110 short period velocimeters (EH). The on-shore part of the AASN was operational for about 4 yr (2016 January–2019 December) and the off-shore part for about six months (2017 September–2018 February).

oceanic basins and platforms including remarkably strong lateral crustal variations from local to regional scales.

Many geophysical and geological studies at various levels of resolution have targeted the Alpine orogeny's structure and evolution (e.g. Schmid *et al*. 2004; Rosenberg *et al*. 2018, and references therein). Nonetheless, many important questions regarding the undergoing geodynamic processes that characterize the European and Adriatic plates interaction and their possible relation with the spatially strongly variable seismicity in the region are still a matter of debate (e.g. Handy *et al*. 2010; Kissling & Schlunegger 2018; Kästle *et al*. 2020; Malusà *et al*. 2021 and references therein).

The compilation of a uniform seismic catalogue in terms of hypocentre locations and magnitude assessment would help in this regard. Obviously, the creation of a homogeneous catalogue represents a great challenge since hypocentre locations and magnitudes differ significantly between several national and regional catalogues in the GAR. It would also be unrealistic to achieve without *a priori* information that allows to correct for the inherent differences in the existing catalogues.

Currently, the GAR regional seismicity is recorded and reported by many national and two international seismic-observatories: the International Seismological Centre (ISC) and the European-Mediterranean Seismic Centre (EPOS-EMSC). Almost a dozen national and local seismic agencies are responsible of reporting the local seismicity (Fig. S1, Supporting Information). Hence, to obtain a reliable, regional data set complete to magnitudes M3, it is necessary to perform a non-trivial catalogue merging (or pairing) process with several individual catalogues (Solarino *et al*. 1997; Rezaeifar *et al*. 2018; Braclawska & Idziak 2019; Mueller 2019; Sawires *et al*. 2019; Rojo Limón *et al*. 2021). The main obstacles faced when establishing a catalogue from individual observatory bulletins are: (1) inconsistencies in hypocentre locations, (2) inconsistencies in

Downloaded from https://academic.oup.com/gji/article/231/2/921/6609778 by OGS (Istituto Nazionale di Oceanografia e di Geofisica Sperimentale-OGS) Borgo Grotta user on 11 December 2023

reported magnitudes and (3) problems to correctly associate individual observations from one network with events reported by another network (e.g. Fig. S2, Supporting Information). These problems also occur for the GAR seismicity-catalogue because each national observatory usually applies different event-location software, filters, picking-algorithms and velocity models. In addition, different magnitude of completeness among the catalogues may occur, increasing the potential of inconsistencies during the pairing processes.

Solving the first of the above-mentioned problems is of equal importance for both earthquake seismology and seismic tomography (Diehl *et al*. 2009c) while solving the second problem is crucial, for instance, for seismic hazard assessment and solving the third problem is key to all kinds of seismic tomography applications. Uniform estimation of earthquakes magnitudes across the GAR is particularly difficult as different local-magnitude formulae and different attenuation functions are adopted by each agency (e.g. Goertz-Allmann *et al*. 2011; Lolli *et al*. 2015; Bindi *et al*. 2019). Furthermore, pairing of events reported by more than one observatory is difficult due to severe heterogeneities and distortions among the individual observatories' permanent network geometries. The goal of this study is to tackle these problems taking advantage of the unprecedentedly large and homogenous AlpArray seismic station network (AASN, www.alparray.ethz.ch) to produce a high-precision and consistent local seismicity-catalogue of the GAR for the time period 2016 January 1–2019 December 31.

Due to the large station array and great data stream production by AASN, conventional seismicity-catalogue processing (e.g. events relocation and magnitude determination) based on manual phase picks and manual results evaluation would be extremely time consuming. Additionally, such processing may also lead to blunders and inconsistencies, for example, in quality assessment as a result of very long and tiring picking sessions. For this reason, we developed a semi-automated procedure to produce a high-precision and consistent seismicity-catalogue. With this automated procedure we aim to translate the conventional routine processing approach of seismic observatories into a multistep processing chain starting from data retrieval up to magnitude determination. Specifically, we try to emulate as much as possible the tasks of the revising experienced seismologist by a series of automated checking and revising steps. We document the successful application of this method in section three.

The resulting final AlpArray Research Seismic Catalogue (AARSC) from 2016 January 1 to 2019 December 31 contains 3293 events of magnitudes larger than 0.4 M_{Lv} within the GAR. This catalogue is complete down to 2.4 M_{Lv} and it is regionally consistent with the different magnitude scale reports $\geq$ 3 (M3+) of events reported by other agencies' bulletins that span the same time period. Our catalogue may well serve as data base for subsequent GAR-wide regional seismic tomography. The AARSC, as confirmed by comparisons with regional and local earthquake bulletins, well delineates the most of the major seismically active faults and seismotectonic features in the region. However, since we consider just a 4-yr period, the catalogue is not representative for the long-term seismicity and, in particular, for the local microseismicity ($<$ 2.5 M_{Lv}) characteristics that vary significantly in time and across the GAR. The documented consistency of this new seismic catalogue underlines the performance and usefulness of the newly developed automated processing for very large seismic station arrays. As additional results of this study and in combination with the AARSC, we present a minimum 1-D *P*-wave velocity model with appropriate station delays (Kissling *et al*. 1994) for all permanent and temporary seismic stations in the GAR. This result represents a pre-requisite to compile a consistent, complete and high-precision earthquake catalogue for both pre- and post-AlpArray times that could, eventually, help improving current seismic hazard assessment in the region (Woessner *et al*. 2015).

2 SEISMIC STATION NETWORK AND DATA QUALITY

Taking advantage of previous Alpine seismology research collaborations, in 2015 a group of about 50 earth sciences university institutions and seismic observatories established an international collaborative research program called AlpArray (www.alparray.ethz.ch). The AlpArray is a large-scale European initiative with the aim to shed new light on the tectonic and geodynamic processes of the Alpine region and neighbourhood Apennines-Carpathians-Dinarides orogens and the related seismicity. The AASN denotes the largest temporary broad-band (BB) seismic experiment ever deployed in Europe, providing new seismological data of unprecedented high quality. The AASN temporary seismic stations complement the existing permanent station networks by the seismic observatories, ensuring a homogeneous station coverage of the GAR ($\sim$1600 km by $\sim$800 km, grey contour line Fig. 1). The geographical distribution of the AASN stations is the results of a hexagonal compact packing strategy (Hetényi *et al*. 2018, fig. 4b). Such a geometry aims to cover the spatial gaps between and within national observatories permanent seismic networks, resulting in an average interstation distance of $\sim$50 km and providing a closest-station distance of $\sim$30 km through the entire GAR (see Hetényi *et al*. 2018, and references therein for detailed information). This is of particular interest in regions like the Po Plain, the central eastern Alps, the northern Alpine foreland, Austria and Germany where heterogeneities in the permanent BB station distributions are more pronounced.

The dense station distribution of AASN greatly increases the resolution potential of any study related to earthquake seismology (e.g. tomography and seismic hazard) and allowing as well the unique possibility of a uniform magnitude assessment for the GAR events.

The seismic network we used in this study consists of total 1103 seismic stations: 849 BB, 144 accelerometer and 110 short-period seismometers. The core of this network are 352 permanent stations across 11 countries, and 276 (including 30 OBS) temporary BB stations (Z3) that form the AASN (as described in Hetényi *et al*. 2018). The on-shore part of the AASN was operational for the 4 yr 2016–2019, and the oceanic part for about six months (2017 September–2018 February, Hetényi *et al*. 2018). To establish a consistent, complete and high precision seismic catalogue for the GAR and to increase the ray coverage specifically in the peripheral regions, we complemented the AASN with permanent short period stations, accelerometers and BB stations inside and also outside the GAR (Fig. 1) leading to the above-mentioned number 1103 stations with data used in this study.

We download the three-component, raw data from all 1103 stations, grouped into 38 different network codes, using the FSDN EIDA webservices (www.orfeus-eu.org) implemented in the ObsPy library (Krischer *et al*. 2015), ending up with a database of $\sim$50 TB. Dealing with such large data set from heterogeneous networks is challenging and time consuming for various reasons: many different sensor's type sensitivities (e.g. seismometers and accelerometers); data and metadata retrieval problems from data centres; issues with stations metadata updates; problems with waveform accessibility

Downloaded from https://academic.oup.com/gji/article/231/2/921/6609778 by OGS (Istituto Nazionale di Oceanografia e di Geofisica Sperimentale-OGS) Borgo Grotta user on 11 December 2023

(either online or offline); stations GPS locations and timing problematics.

Moreover, the data set is extremely variable in terms of data availability, completeness and data quality at each station. To quantify how much a station contributes to our analysis, we calculated the data availability per year, per station (Fig. S3, Supporting Information) and, to overall check the data, we computed the probabilistic power spectral densities (PSD) for each station for the whole period (Fig. S4, Supporting Information). Our data set (vertical components only) shows a simultaneous data availability that varies through the years and with regional variation: 74.8 per cent in 2016, 81.3 per cent in 2017, 76.3 per cent in 2018 and 70.8 per cent in 2019. These numbers are mainly affected by the different installation and dismantling dates of the temporary stations (e.g. stations in France were installed starting from 2017; stations in Croatia and in NE Italy were dismantled during the first half of 2019). Consequently, the geographical distribution of stations with less than 50 per cent of data acquired per year is also variable, with a poor coverage in the westernmost GAR during 2016.

The PSD plots are helpful to detect problems with data availability, errors in the metadata, to quantify the overall background noise level as a function of frequency at each site and to detect station operation artefacts. We compute them using the direct Fourier method (Cooley & Tukey 1965) based on the routine implemented in the ObsPy software (McNamara & Buland 2004; Krischer *et al*. 2015). In Fig. S4 (Supporting Information), we compare the median of the 4-yr long PSD from the temporary stations (Z3) with the permanent one (only BB sensors). As a general consideration, the temporary stations perform similarly to the permanent ones for period > 1 s and show a higher median noise level for period < 1 s ($\sim$10 dB) although remaining in most cases below the maximum allowable AlpArray noise level. Of course, the PSD variation strongly depend on the station site both geologically and geographically and on the installation technique (e.g. Fuchs *et al*. 2016; Molinari *et al*. 2016; Govoni *et al*. 2017; Vecsey *et al*. 2017, Gráczer *et al*. 2018; Petersen *et al*. 2019). The PSD plots (Fig. S4, Supporting Information) confirm the general high quality of the temporary installations, well suited for almost all seismological applications. The higher noise level at shorter periods is mainly due to installations at sites in densely populated regions. These areas are usually avoided by seismic observatories for permanent stations because of the well-known anthropogenic high-frequency noise (e.g. Po Plain in Italy). This analysis, however, does not account for the usually short periods of malfunction of individual stations that obviously also affect the local sensitivity of the AASN through time.

3 AUTOMATED EARTHQUAKE DETECTION AND LOCATION PROCEDURES

Standard seismic monitoring software like the SeisComP3 (SC3, Hanka *et al*. 2010) or the EarthWorm (EW, Johnson *et al*. 1995) frameworks automatically generate preliminary events catalogues. The manual revision of these catalogues is one of the most time-consuming steps in seismological observatory practice. While automatic event detection, phase association and event location are crucial for real-time applications such as earthquake early warning, these algorithms can fail and generate erroneous detections (e.g. 'fake events') or lead to gross errors in hypocentre location and magnitude computation. The review of such preliminary automatic solutions therefore requires a manual revision by an experienced human analyst to ensure a high quality of the earthquake bulletin. During this review process, which is routinely performed in most seismological observatories, the analyst usually checks each phase arrival individually at different stations to make sure the same phase is consistently and correctly identified through the network, especially for questionable automatic solutions (e.g. locations with large azimuthal gap angle (GAP), a large magnitude associated with only few observations, or locations associated with unusually high root-mean-square (RMS) values). The analyst performs manual re-picking of phase arrivals and subsequent hypocentre relocation. Such careful analysis will identify and remove fake detections from the catalogue and also assign event-type classification to non-seismic sources (e.g. landslides, quarry blasts and explosions), therefore leading to a high-quality earthquake bulletin. In times of high workload (e.g. in cases of intense earthquake sequences or large magnitude events with large number of recordings), however, human errors or inconsistencies between different people sharing the work may occur during the analysis process.

As a consequence, the processing of $\sim$50 TB waveforms data would benefit from applying automatic event detection, observation and event outlier detection, and location algorithms. These would eventually improve the final consistency and provide a more uniform error assessment throughout the process. The preliminary automatic catalogue derived from the application of the SC3 software to this data set (described in detail later) includes nearly 40 000 events, which makes the manual review unfeasible and requires sophisticated, automated tools for assessing the quality of automatic solutions and eventually refining them.

To compute a reliable, high-quality earthquake catalogue of the GAR, we therefore developed and validated a modular, iterative and fully automated offline procedure, which is summarized in Fig. 2. This workflow is specifically designed to mimic as much as possible the decision-making stages that expert analysts usually adopt in manual revision.

Thus, the production workflow for the AARSC makes use of three software packages, the SC3 seismic monitoring system, the newly developed ADAPT picking library (Bagagli 2022), and the VELEST location algorithm (Kissling *et al*. 1995) that features a joint-hypocentre determination (JHD) location method. The processing to obtain the AARSC is divided into eight stages and the workflow is as follows (see also Fig. 2):

(i) Step 1: calculation of an automatic earthquake catalogue by applying SC3 offline to the raw waveform data collected at the AASN during the period 2016 January–2019 December. This results in a preliminary event list, providing hypocentres and local magnitudes [1 month of catalogue in $\sim$12 hr, multicore 2.5 GHz].

(ii) Step 2: primary event quality assessment and filtering to clean SC3 preliminary event list from erroneously associated events ('fake events'). [$\sim$10 hr/100 events, single-core 2.2 GHz]

(iii) Step 3: 1st round of re-picking all possible phases including first-arrival consistency analysis with ADAPT library. [$\sim$9 hr/100 events, single-core 2.2 GHz, depending on the amount of features extraction and tests applied]

(iv) Step 4: 1st round of phase and event quality filtering by JHD processing as part of VELEST software. Consistent high-precision hypocentres re-locations based on minimum 1-D model and appropriate station delays to improve first arrival-time predictions used in step 5. [$\sim$8 hr, single-core 2.50 GHz]

Downloaded from https://academic.oup.com/gji/article/231/2/921/6609778 by OGS (Istituto Nazionale di Oceanografia e di Geofisica Sperimentale-OGS) Borgo Grotta user on 11 December 2023

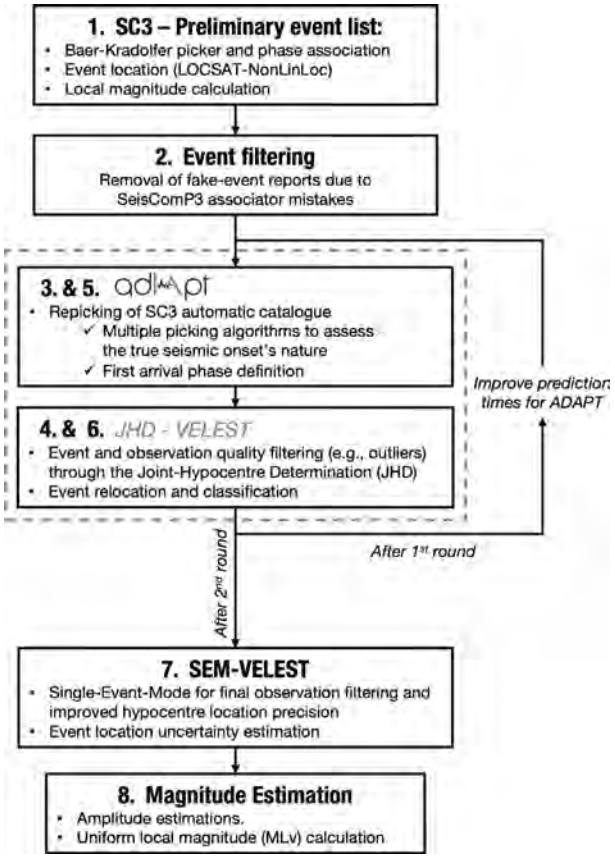

Figure 2: Detailed production workflow for the AlpArray Seismicity Research Catalogue (AARSC) compilation. This workflow successfully replaces the standard manual checking and revising by experienced seismologist from steps 2 to 8, performed by specifically designed software in offline mode. The SC3 software used for the preliminary event list compilation internally creates different event origins: preliminary ones with LOCSAT (Bratt & Nagy 1991), and refined ones with NLL (Lomax *et al*. 2000). Please refer to Section 3 of the main manuscript and Text T1–T2–T3 in the Supporting Information for the workflow's details.

(v) Step 5: 2nd round of re-picking all possible phases including first-arrival consistency analysis with ADAPT library. [∼9 hr/100 events, single-core 2.2 GHz, depending on the amount of features extraction and tests applied]

(vi) Step 6: 2nd round of phase and events quality filtering through the JHD processing. [∼8 hr, single-core 2.50 GHz]

(vii) Step 7: final consistent and high-precision hypocentres relocation using VELEST single-event mode (SEM) including an iterative phase filtering for outlier detection based on studentized residuals (e.g. Pope 1976; Kissling 1988; Sohn *et al*. 1997). In this step we also quantitatively assess the final location uncertainty. [∼0.2 hr, single-core 2.50 GHz]

(viii) Step 8: S-phase amplitude estimations on vertical component seismograms for Richter local magnitude re-calculation, MLv (Richter 1935, Hanka *et al*. 2010) [∼0.3 hr/100 events, single-core 2.2 GHz]

We employ two rounds of ADAPT-JHD-VELEST picking, quality filtering and hypocentre location (above steps 3 and 4 denote the 1st round and steps 5 and 6 denote the 2nd round) in order to provide higher consistency and higher precision to our catalogue. A stepwise description of the workflow will follow in the next sections.

3.1 Creation of SC3 preliminary seismicity-catalogue (step 1)

The SC3 software is a widely used seismic-network monitoring tool, which is also adopted by a few observatories in the GAR. It is used to generate the initial preliminary earthquake catalogue, as it provides all necessary algorithms for automatic detection, location and magnitude estimation of seismicity from local to regional scales. In addition, it is fully compatible with the infrastructure provided by the EIDA archives hosting the AASN data used in this study. Thus, integration of waveform and station metadata of the AASN into the SC3 system is straightforward. Another advantage of using SC3 for the preliminary catalogue generation is that results are stored in a well-defined database, which allows convenient manual review of automatic solutions using SC3's graphical user interfaces as well as dissemination (e.g. via FDSN web services) and export to modern seismological formats such as QuakeML (Schorlemmer *et al*. 2011). Although SC3 is mainly used for real-time monitoring purpose, it could also be applied to waveform archives to generate high-quality earthquake catalogues in offline mode (e.g. Diehl *et al*. 2017).

The SC3 setup used for offline processing of the AASN data follows largely the procedure and parameters described in Diehl *et al*. (2017). The large number of stations included in the AASN, however, required several modifications in the procedure (details on the configuration and procedures used for the AASN are provided in Text T1 in the Supporting Information). Initially, an STA/LTA-based *P*-phase detector was combined with the Baer–Kradolfer (BK) picker algorithm (Baer & Kradolfer 1987) in SC3's *scautopick* module (see Supportig Information T1 for details on this procedure), which was applied to vertical components of all stations (Fig. 1), subdivided into several parallel sub-processes (per station, per day). After the picking-stage was completed, all automatic picks were chronologically ordered and arranged into daily chunks. The daily chunks were then fed into SC3's *scautoloc* module, which performs event detection by associating the phase picks to origins. The module generates a multitude of origin solutions similar to SC3's real-time mode, each provided with a first location using the *LOCSAT* location algorithm (Bratt & Nagy 1991) with a global velocity model (*iaspei91*, Kennet 1991). Each of the generated origins was then refined by the module *screloc*, using the probabilistic *NonLinLoc* (NLL) location algorithm (Lomax *et al*. 2000) with the equal-differential-time (EDT) method (e.g. Font *et al*. 2004) in combination with the 1-D Alpine model of Diehl *et al*. (2009a). The EDT method is more robust in presence of outliers caused by automatic picking as well as velocity model errors (e.g. Font *et al*. 2004). Finally, the module *scmag* computed a preliminary M_{Lv} magnitude for each origin solution. The M_{Lv} magnitude is a local magnitude that use the original attenuation relationship of Richter (1935). The peak amplitude of M_{Lv}, however, is measured on the vertical component. Based on origin time, location and arrival-time picks, the different origin solutions were then associated to an event by the *scevent* module. To select the preferred origin among the different origin solutions associated to an event, we implemented a location-quality score function in the *scevent* module (see Text T1 and T2 in the Supporting Information). This score value considers (1) distribution of residuals, (2) location GAP, (3) distance to closest observing station and (4) number of observations to select the best event's origin location. The event-score value provides additional information on the location quality and was used for downstream quality filtering to remove potential erroneous locations or fake detections as described later. The proposed

Downloaded from https://academic.oup.com/gji/article/231/2/921/6609778 by OGS (Istituto Nazionale di Oceanografia e di Geofisica Sperimentale-OGS) Borgo Grotta user on 11 December 2023

procedure reduces the playback time significantly and thus the processing of ∼1000 stations for a 1-month period of the catalogue requires about 12 hr including waveforms re-picking, phases association and events location.

The preliminary catalogue (SC3-PC) is composed of 39 603 events and 731 601 *P* observations, with magnitudes ranging between 0.2 and 6.7 M_{Lv}. Magnitude is unknown for a subset of 627 events where the computation failed for various reasons (e.g. insufficient number of amplitudes above signal-to-noise threshold, erroneous or incomplete instrument responses in station metadata). Fig. S5 (Supporting Information) shows the epicentral distribution of the SC3-PC catalogue, which represents the starting point of our automatic filtering scheme and location refinement procedure (steps 2–8 in Fig. 2) described in the following sections. No automatic event-type classification was performed for the SC3-PC catalogue. It therefore can contain a certain number of anthropogenic sources (e.g. quarry blasts or induced seismicity). However, the contamination of quarry blasts for the targeted magnitudes ≥2.4 is expected to be very low. Similarly, the number of anthropogenically 'induced' earthquakes in this magnitude range is likely very low in the GAR.

3.2 Event filtering stage (step 2)

The SC3-PC catalogue (Fig. S5, Supporting Information) contains erroneously detected (fake) events (e.g. see Fig. S6, Supporting Information) that could either result from erroneous picks (e.g. mixture of first-arriving *P* and later-arriving phases such as *PmP* or *S*-phases) or from erroneous phase association (e.g. associated with local noise-bursts or concurrent occurrence of two or more events within the network), leading to a false origin's declaration. Hence, to identify and remove low-quality locations, erroneous detection and events outside the region of interest from the preliminary catalogue, we propose an *a priori* event-quality filtering. Defining appropriate quality thresholds, however, is difficult, since we want to avoid rejecting any possibly 'real' earthquake of magnitude $M \geq 2$. Especially for larger magnitude earthquakes, which are part of a sequence of events with short interevent times, 'unguided' automatic picking can lead to mixing of phases from separate events into one single event. Therefore, the proposed quality filtering of events and phase picks in steps 4 and 6 is designed to identify and correct such cases.

In order to remain in the candidate list for further refined processing, an event in the SC3-PC catalogue must meet all the following criteria: (i) epicentre location within the GAR boundary (grey contour line in Fig. 1), (ii) local magnitude $M_{Lv} \geq 2.0$, with the exception of events of unknown magnitude (attempt to recalculate them in step 8) and (iii) event location-quality score value (≥−2) (Text T2 in the Supporting Information). Although this event score parameter is directly related to the location quality (e.g. GAP, RMS, number of observations), it turned out to be insufficient to identify all problematic events. To take advantage of the rather uniform station spacing of the AASN (Fig. 1), we therefore introduced an additional fourth criteria, which evaluates a parameter called (iv) *closeratio*. This parameter relates the number of observations reported by SC3 for any specific event with the number of stations operated at the time within an a priori defined radius around the epicentre. Since first *P* arrival observations are either of type *Pg* or *Pn* we define a radius of 80 km (*Pg*) and a second radius of 300 km (*Pn*). An event is considered real and passed on to the final event list if the parameter *closeratio80* is equal or larger than 0.5 (e.g. at least 50 per cent of all possible stations yielded useful observations for SC3). For events with magnitude smaller than M_{Lv} 2.5, we accept a *closeratio80* of 0.4 or higher. Sometimes for events of medium to larger magnitudes the first arrivals at nearby stations are difficult to pick for SC3 and the set of observations may be dominated by *Pn* arrivals at more distant stations. To account for such cases, we also accept events with a *closeratio80* equal or better than 0.2 in combination with a *closeratio300* equal or better than 0.5. Applying all the four criteria to the 39 603 events detected by SC3 we end up with the final SC3 event list containing 3392 events located within the GAR during period 2016–2019 (Fig. 3) that will be processed further. For the full, detailed, stepwise event filtering process, the reader is referred to the Text T3 in the Supporting Information.

3.3 Individual phase re-picking stage (steps 3 and 5)

The unprecedented large number of waveforms potentially available for the 3392 events from the 1000+ station array during the time period 2016–2019 makes the manual checking and re-picking of events unfeasible. For this reason, we developed a specific picking software named ADAPT aiming to properly identify and pick the first arrival *P* waves (Bagagli 2022). The re-picking approach relies on a combination of five different automatic high-quality *P*-wave pickers that provide precise and consistent observations of seismic first arrivals with an associated error estimate. The waveform preprocessing consisted of a linear detrend, demean and Butterworth two-poles band-bass filter 1–30 Hz. Similarly to step 2, for ADAPT stages we split our data set in chunks of 100 events to parallelize the workflow on a cluster.

Within the ADAPT multipicking modules, we exploit the sensitivities (characteristic functions, CF) of five different well-established picking algorithms. By combining these pickers, we aim to detect seismic arrivals in waveforms when the signals exhibit changes both in time and frequency properties. The pickers chosen are (1) the BAIT picker (Bagagli *et al*. 2020, supplementary), (2) the BK (Baer & Kradolfer 1987), (3) the Akaike-Information-Criteria (as developed in Maeda *et al*. 1985; Bagagli 2021a), (4) the Filter-Picker (Lomax *et al*. 2012; Bagagli *et al*. 2019) and a (5) High-Order-Statistic based picker (Saragiotis et al. 2002; Küperkoch et al. 2010; Baillard et al. 2014; Bagagli 2021b). ADAPT also allows a multislicing approach where the user may select different picking-time windows for each picker separately. Analogue to other picking algorithm developments (e.g. Baer & Kradolfer 1987; Alderson 2004; Diehl *et al*. 2009b) we tune the individual picking-algorithms using manually picked *reference dataset* composed of 11 events with an SC3-$M_{Lv} \geq 3.0$ and a total of 1373 *P* phases.

The reasons behind this approach are:

(i) Each single picking algorithm calculates a specific CF defined by the internal properties of the time-series itself. These could be either frequency-dependent, statistics dependent, amplitude dependent or phase-dependent. Therefore, each picker is sensitive to different features in order to declare a valid phase arrival.

(ii) Timing observations are more stable and statistically more reliable by having several reads for same arrival (see also Diehl *et al*. 2009b; Küperkoch et al. 2010).

(iii) Each single picker will likely detect the wavelet onset at slightly different times, thus providing useful information about the observation uncertainty (see also Diehl *et al*. 2009b; Küperkoch *et al*. 2010) and the true nature of the onset.

(iv) The use of two different time windows (slices) for each picker increases the chances to pick the correct phase onset by allowing to detect and thus mitigate outlier picks.

Downloaded from https://academic.oup.com/gji/article/231/2/921/6609778 by OGS (Istituto Nazionale di Oceanografia e di Geofisica Sperimentale-OGS) Borgo Grotta user on 11 December 2023

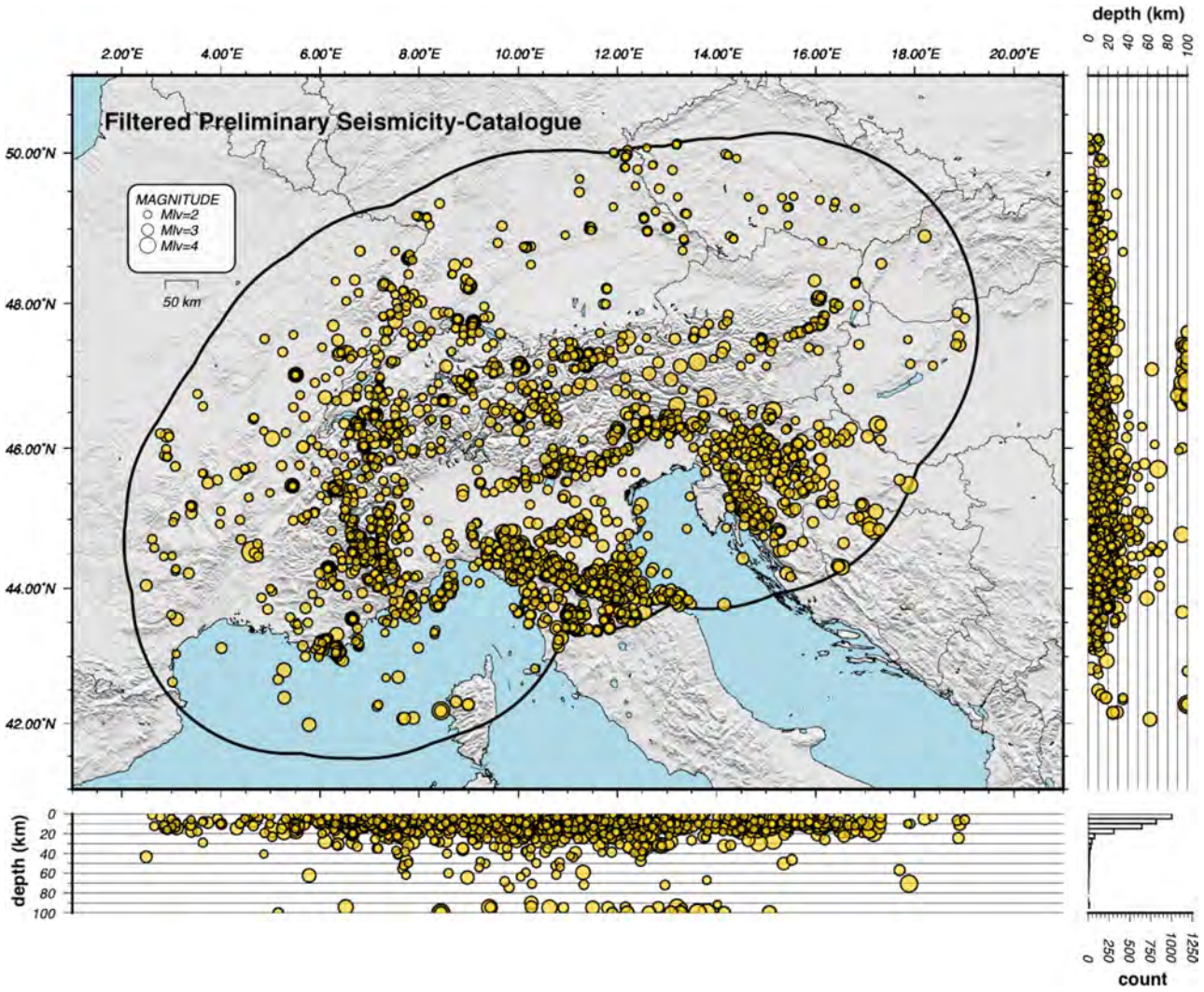

Figure 3: Seismicity after event filtering for quality and plausibility of step 2. A total of 3392 events are located inside the GAR. For plotting clarity, 16 events with a depth ≥ 100 km are projected to 100 km.

The ADAPT procedure aims to reflect the different evaluation and estimation processes applied by experienced seismologists during the picking stage of the individual waveforms. An example of the successful application of the ADAPT re-picking system is displayed in Fig. S7 (Supporting Information). For further details of the automated ADAPT picking procedure and the tuning stage please refer to Bagagli *et al.* (2022).

For each event in our list, we loaded all vertical component waveforms from stations located inside a pre-defined radius from the epicentre location, based on the preliminary SC3 M_{Lv} assigned to the event. We extract data up to 300 km radius for events with $M_{\mathrm{Lv}} < 3.0$ or unknown magnitudes, up to 450 km for events with $3.0 \leq M_{\mathrm{Lv}} < 4.0$ and up to 600 km for events with $M_{\mathrm{Lv}} \geq 4.0$. The reasoning of such a wide-range selection is not primarily related to the event location purposes, but also to the collection of potentially valid observations for other seismological studies as well (e.g. traveltime tomography). The time window of the analysis for each waveform is linked to the event-origin time (OT) and the epicentral distance (ED) in km: we select data between $[\mathrm{OT} - 10\mathrm{s},\ \mathrm{OT} + {}^{\mathrm{ED}}/_{2.2\ \mathrm{km/s}} + 30\ \mathrm{s}]$. We apply this data-selection scheme in both steps 3 and 5 of our workflow (Fig. 2).

3.4 Observation and event outlier detection and hypocentre relocation stage (steps 4 and 6)

During the manual review of an event, the seismologist usually analyses each individual observation comparing phase moveout and consistency across the different waveforms. Hypocentre relocation and critical assessment of arrival-time residuals and event RMS residual are also part of this analysis. We replicate such assessment by applying in our workflow the VELEST software (Kissling 1988) with the purposes to identify observation outliers and problematic events through the JHD. We also use the VELEST algorithm to consistently relocate hypocentres using the minimum 1-D model approach (for more details, see Bagagli 2022). The JHD processing allows to compare the ensemble of all data with every individual observation and with every individual event. Thus, individual observation outliers may be recognized independently from the event location residual by a comparison with all other observations from the same station, even providing quantitative uncertainty estimates (Husen et al. 1999, 2011; Pujol 1988, 2000; Maurer *et al.* 2010). The coupled JHD-velocity inversion, with a minimum 1-D velocity model as initial model, guarantees consistent and uniformly precise hypocentre locations for all well-locatable (WL) events. The

Downloaded from https://academic.oup.com/gji/article/231/2/921/6609778 by OGS (Istituto Nazionale di Oceanografia e di Geofisica Sperimentale-OGS) Borgo Grotta user on 11 December 2023

observation residuals for all phases observed at the same seismic station should not vary significantly more than the overall average data variance (Kissling et al. 1994; Rojo Limón *et al.* 2021). For outliers' detection we define a threshold of ±1 s. We choose this value because the first arrivals of local earthquakes are, on average, within epicentral distances up to 200 km. Thus, an arrival time difference of 1 s or more usually refers to a different seismic phase. For some observations at larger epicentral distances (e.g. -*Pn*) such threshold is likely too strict for regions characterized by complex 3-D Moho topography, like some parts of the Alps (Spada et al. 2013). Nonetheless, we use this value since *Pn* phases that travelled across complex 3-D Moho topography do not really add useful constraints to the hypocentre location. Obviously, for other studies such as seismic tomography, these observations could become very useful and, consequently, the filter definitions would need to be adjusted. If an observation residual relative to the average station delay exceeds this limit, it is deemed an outlier and it will be disregarded for subsequent high-precision hypocentre location.

When applying the ADAPT software, we assume the correct association of the waveforms to an event, and the performance of the automated picker depends on a good prediction of the time windows that implicitly result from precise and reliable event locations. Many poorly located events, or even a few fake ones, might still be expected to remain in our final SC3 event list (see Section 3.2). After identifying and deleting outlier observations and problematic events from the data set, we re-locate all remaining events with the minimum 1-D model. Then a second round of re-picking by ADAPT software is initiated using the improved hypocentre locations and the appropriate station delays to calculate more realistic arrival time predictions (step 5, Fig. 2).

The benefits of applying two rounds of re-picking and quality filtering for observations and events are documented in Fig. S8 (Supporting Information) by comparing the results after the first round (steps 3 and 4, Fig. 2) with those obtained after the second round (steps 5 and 6, Fig. 2). As a main result, in the second round, we pick and recover a total of 4919 more observations, reducing also the azimuthal GAP for the majority of our events (Fig. S8a, Supporting Information).

At the end of stage 5 (re-picking), we adopt a first-order classification scheme for the observed picks. We calculate the time residual between the valid ADAPT pick and the predicted arrival time after step 4 that includes relocated hypocentre, ray tracing through the minimum 1-D model and the respective station delay. If the residual is >1 s and the phase was observed at a station with a reliable delay (estimated with at least 20 observations from different events) we downweight the observation by a factor of 2 for the subsequent event location stages.

3.5 Single-event-mode filtering and final location (step 7)

After the final JHD calculations of step 6 (Fig. 2), we classify the events in three different quality groups:

(i) WL: these events show $N\_P_{\mathrm{obs}} \geq 7$ and GAP $< 180^{\circ}$.
(ii) PL: these events show GAP $\geq 180^{\circ}$ or $4 < N\_P_{\mathrm{obs}} < 7$.
(iii) VPL: these events show $N\_P_{\mathrm{obs}} = 4$.

Even after two rounds of ADAPT-JHD-VELEST processing, principally WL events might show biased hypocentre locations due to a single or few erroneous observations with traveltime residuals up to 1 s. Note, however, that such observations are below the threshold of the JHD individual observation quality filtering and were not removed in previous steps 4 and 6. In most cases of WL events with many observations, this bias may only affect the hypocentre's depth, while poorly locatable (PL) and very poorly locatable (VPL) events may be affected by single or few erroneous observations in all hypocentre parameters.

To identify and subsequently ignore such problematic observations for final hypocentre locations, all events are relocated with the VELEST program in SEM (Kissling et al. 1995), allowing that each observation is individually evaluated based on the importance to the solution and the studentized residual (e.g. Pope 1976; Sohn *et al.* 1997). We use this latter statistical parameter to determine the individual observation leverage (or influence) for the inversion stability. We compare the individual observation's residual with the standard deviation of the overall residuals, therefore detecting gross outliers. We obtain such value by randomly removing one observation's residual and dividing it by the left-one-out residual's standard deviation. If the studentized residual is large (>0.5 or < −0.5 s) compared to the assumed maximum picking uncertainty of ±0.3 s and if the importance of this observation is also relatively large (0.1 or larger), the hypocentre location may show a significant bias. Even if the importance is smaller than 0.1, an observation with a studentized residual larger than ±0.5 s may potentially lead to a more erroneous hypocentre location than the one estimated for the average data noise. Thus, such large studentized residual most likely indicates a phase identification error. For this reason, we decided to remove from each event all observations with studentized residuals larger than ±0.5 s. Since the removal of such observations might cause significant origin time shift, the process of SEM relocation is repeated until no studentized residual larger than ±0.5 s remains (for more details, see Bagagli 2022). During this SEM relocation step we ignored observations at stations beyond 300 km epicentral distances because phases recorded at those distance have a greater chance of being wrongly identified and, considering the uniformly dense station array used in this study, they do not really improve the location.

In order to maintain the consistency and filtering logic of our procedure, we prefer the linearized approach of VELEST compared to other nonlinear algorithms, like the NLL software (Lomax et al. 2000). The main reasoning stands not in the event-location method differences per se, but rather in the location error assessment approach both at the event and single-phase level. NLL uses a Monte Carlo approach to obtain a probability density function for the event location, describing all the possible hypocentre positions for the same phase set (Lomax et al. 2000). On the other hand, iterative-linearized location programs (like VELEST) produce a single-point solution for the preferred hypocentre, providing uncertainty estimates based on Gaussian, or normal, statistics. In fact, such a solution would be a good representation of the complete, probabilistic location only for cases where the density function has a single optimum and a near-ellipsoidal form. For WL events we indeed assume a similar convergence for the two approaches because of the higher constraints provided by the larger set of travel time observations. For PL events, instead, a nonlinear approach would better describe the ill-posed location problem, although it would still require an *a posteriori* careful manual check by the operator. Additionally, as we only use a first-order observation weighting (see Section 3.4), the location inversion process of NLL would be strongly biased by outliers. The weighted least-square approach used in VELEST-SEM is also sensitive to outliers and for such algorithm, the fastest and reliable way to declare them as such is using the studentized residual (Sohn *et al.* 1997).

Downloaded from https://academic.oup.com/gji/article/231/2/921/6609778 by OGS (Istituto Nazionale di Oceanografia e di Geofisica Sperimentale-OGS) Borgo Grotta user on 11 December 2023

As a result, it may happen that a previously classified WL actually became a PL, a VPL or even being rejected due to fewer than four observations remaining. The 'opposite' is less likely but still possible where an original PL event (with GAP $> 180^{\circ}$) could result in a WL event. An example of such a case (PL $\rightarrow$ WL) is documented in Fig. S9 (Supporting Information) where an event location just beyond the limits of the seismic network (step 6, Fig. 2) is improved in azimuthal GAP by a shift in epicentre after the removal of four observations at distant stations with residuals larger than +/-0.5s.

To quantitatively assess the final hypocentre uncertainties of the WL events we apply a hypocentre shift-recovery test (Haslinger et al. 1999; Husen *et al*. 1999). We shift the final catalogue's hypocentres by 5 km in longitude, latitude and depth, taking care to shift an equal number of events toward W as toward E, same regarding the N-S directions and an equal number to shallower and to greater depth. This new event data set is subsequently relocated with VELEST JHD method with a strong damping applied for the minimum 1-D model. We then compared the original hypocentre locations (results of step 7) with the recovered locations after the VELEST coupled inversion. Assuming the 95 per cent confidence intervals as representative, we obtain location uncertainty estimates of ± 0.7 km for the epicentres and ± 2 km for the hypocentre depth (Fig. S10, Supporting Information). In Fig. S11 (Supporting Information),we present a comparison of the RMS distributions of our final AARSC and of the respective initial SC3 (step 1) events locations. This comparison documents a reduction of the mean-RMS from initial 0.26 s to final 0.19 s and the standard deviation from 0.15 to 0.05 s.

3.6 Magnitude re-calculations (step 8)

The final step of our automatic workflow consists of the final magnitude assessment for all relocated events within the GAR. Step 8 completes the routine processing of the consistent and precise earthquake catalogue allowing to characterize the seismic activity across the GAR. To maintain consistency with the previous SC3 magnitude calculations (step 1, Fig. 2), we implemented an analogous algorithm, attenuation function, and same magnitude scale in our ADAPT library. We adopted the $M_{\rm Lv}$ Richter local magnitude scale (Richter 1935) measured on the vertical component only (https://www.seiscomp.de/doc/apps/global_mlv.html) using the original attenuation functions. The re-calculation of the $M_{\rm Lv}$ magnitudes for the AARSC events is necessary for two main reasons. Primarily, we have different observations and hypocentre locations for each event. Secondly, for nearly 15 per cent of all events the SC3 algorithm was unable to calculate the local magnitude because of too few observations available or due to metadata errors. An additional filtering was applied upfront the Wood–Anderson conversion, with a Butterworth four-poles bandpass filter 1–50 Hz. Furthermore, while the SC3 original station's magnitude estimation are based on the positive peak amplitude, ADAPT magnitudes are based on the mean amplitude from the absolute maximum and minimum values of the waveform. This simple but effective calculation, will allow our system to lower the effect of possible spike transients occurring in the estimation time window, therefore mitigating its effect at the station-magnitude level. We finally measure the wave amplitudes up to 300 km epicentre distances and estimate the event $M_{\rm Lv}$ selecting the stations magnitude median.

To assess the uncertainty of the calculated magnitudes, we plot the distribution of the magnitude residual for each individual observation in relation to the median for the event (Fig. S12a, Supporting Information). Observations with residuals larger than 2 median absolute deviation (MAD) estimated as ± 0.37 $M_{\rm Lv}$ are deemed as outlier observations and are ignored for further calculations. After the removal of the outlier observations, we repeat the events magnitude median calculations with the remaining observations (Fig. S12b, Supporting Information). The final stations residual MAD is measured as ± 0.13 $M_{\rm Lv}$ and it is considered an estimate for our final event magnitude uncertainty (Fig. S12b, Supporting Information). As qualitative classification scheme we use the number of stations (observations) used to calculate the final event magnitude and the single event MAD. All the events with 20 or more observations and a MAD < 0.19 (95 per cent of final events MAD distribution, Fig. S12c, Supporting Information) are considered as class A, all the others are classified as class B. For class A events, we consider the magnitudes to be reliable with an uncertainty estimated by the single event's magnitude MAD, while for class B we add a *penalty factor* equivalent to the inverse number of observations (EventMAD + 1/UsedObs). By doing so, we increase the error associated to events magnitude calculated with few observations. Indeed, a higher MAD obtained by few observations could indicate problematic measurements, while still a higher MAD but determined with many observations is more likely to belong to the real event magnitude.

4 RESULTS: THE ALPARRAY RESEARCH SEISMICITY-CATALOGUE (2016–2019)

The AARSC (2016–2019) in total comprises 3293 events ranging in magnitude between 0.4–4.9 $M_{\rm Lv}$ (Fig. 4). Of these, 2869 events are WL ($N\_P_{\rm obs} \geq 7$ and GAP $< 180^{\circ}$), 387 PL (GAP ≥ 180 or $4 < N\_P_{\rm obs} < 7$) and 37 VPL ($N\_P_{\rm obs} = 4$) events, of which 1145 have magnitude quality class A and 2144 magnitude quality class B (see Section 3.6). For four events (3 VPL and 1 PL) it was not possible to declare a valid magnitude due to the low number of observations. Note that in processing step 2 (Fig. 2) we selected from the SC3 preliminary event list those events inside the GAR with magnitudes equal or larger than 2.0. However, SC3 was unable to obtain magnitudes for 524 events located inside the GAR and if they fulfilled the other quality requirements, these events were also accepted for further processing. In processing step 8 all magnitudes were re-calculated for final epicentre coordinates using re-evaluated individual amplitude observations leading to some events with magnitude values lower than 2.0.

The results of the hypocentres shift-testing (Haslinger *et al*. 1999; Husen *et al*. 1999) suggest a high average precision for all WL events in our catalogue (Fig. S10, Supporting Information, ± 0.7 km for longitude and latitude and ± 2 km for the depth). Taking advantage of the GAR wide consistent high precision hypocentre locations, we may pair the M3+ events contained in the AARSC with those reported by the individual observatory catalogues for the same time period. For this purpose, we obtained from each of the 11 national seismic observatories cover parts of the GAR (Fig. S1, Supporting Information) seismic bulletins from 2016 to 2019 including all events with a magnitude reported equal or higher than 2.5. Note that while in the AARSC catalogue we used a uniform magnitude scale for the entire GAR, the magnitudes reported in the individual catalogues of different observatories might differ to a certain degree (see below). For a completeness check of the AARSC we first pair every M3+ event reported in the individual catalogues inside the GAR with all our AARSC events (including those of

Downloaded from https://academic.oup.com/gji/article/231/2/921/6609778 by OGS (Istituto Nazionale di Oceanografia e di Geofisica Sperimentale-OGS) Borgo Grotta user on 11 December 2023

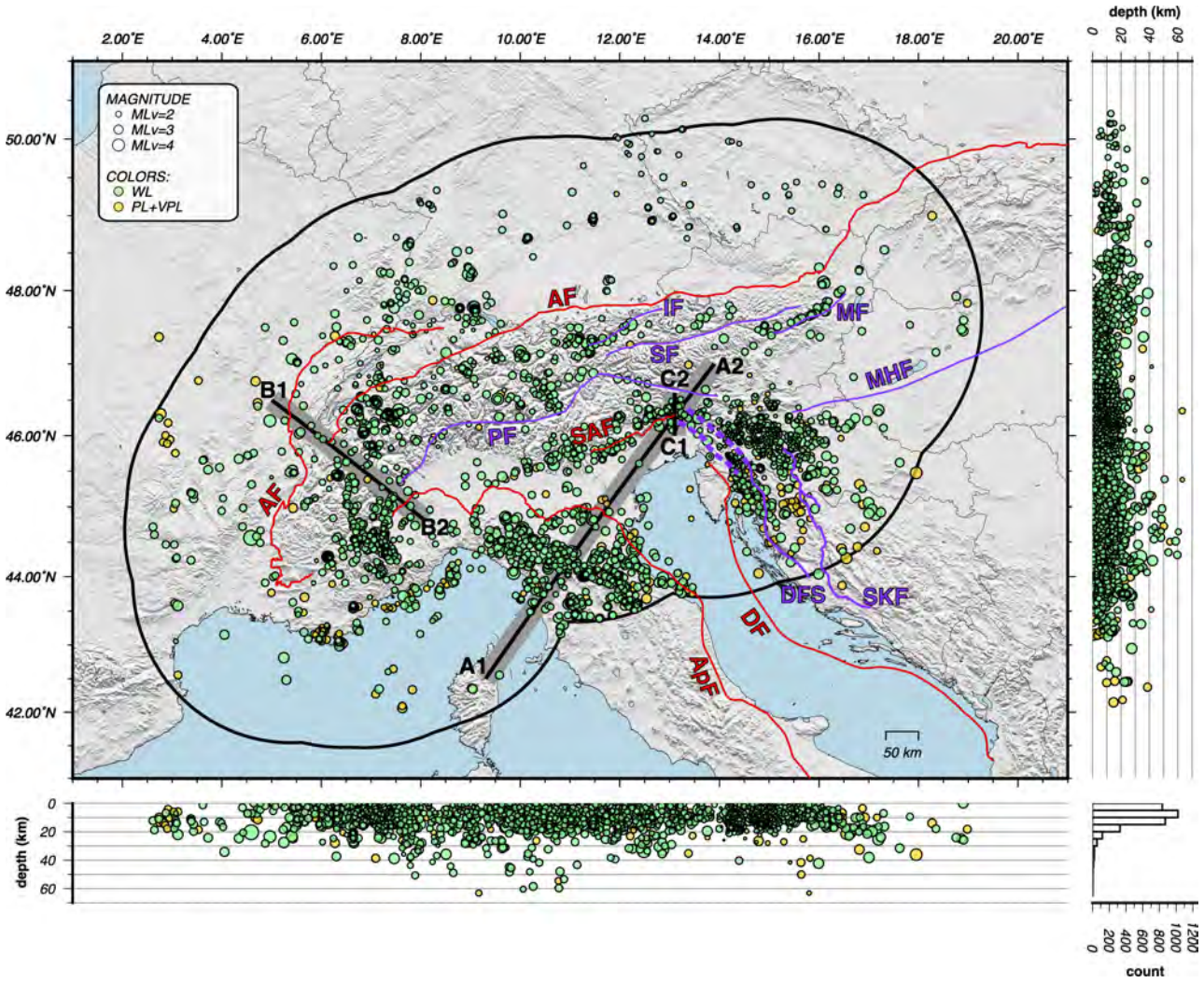

Figure 4: The final AARSC for the time period of 2016–2019. The catalogue encompasses 3293 events, 2383 of those with magnitudes equal or larger than 2.0 M_{Lv}. Filled green circles represent the WL events; filled yellow circles represent the PL and VPL events (see the main text for details). The distribution of the four-year seismicity highlights the main seismically active areas of the GAR. Orogenic fronts (red lines) and major tectonic lineaments (purple lines) simplified from Schmid *et al*. (2004, 2008), Handy *et al*. (2010) and Kästle *et al*. (2020). AF: Alpine front, SAF: southern Alpine front; ApF: Apenninic front; DF: northwestern Dinarides front (Handy *et al*. 2010). The catalogue documents recent activity along a few specific segments of major faulting systems (see the text). PF: Periadriatic faults system; IF: Inntal fault (Reiter *et al*. 2003, and reference therein), SF: SEMP fault (Rosenberg & Schneider 2008; Frost *et al*. 2009, and references therein), MF: Mur-Mürztal faults system (Lenhardt *et al*. 2007), MHF: Mid-Hungarian faults system (Csontos & Nagymarosy 1998), SKF: Split- Karlovac transpressive zone (Chorowicz 1970), DFS: Dinaric faults system (Schmid *et al*. 2004) where NE dashed branch represent the Idrija fault and the NW dashed branch represent the Rasa fault (Grützner *et al*. 2021). Locations shown of three profiles across the northern Apennines (A1–A2), western Alps (B1–B2) and southern Alpine front (C1–C2) presented in figure 6.

lower magnitudes) using a maximum origin time window of 60 s and a maximum distance between epicentres of 150 km. With these settings, we are able to obtain a regional consistently paired M3+ catalogue (Fig. S13, , Supporting Information) apart from eight exceptions, that are discussed and explained in details in Text T4 of the Supporting Information. For the final AARSC we could reprocess six of these exceptions by going through a manual re-pick and subsequent re-location (Text T3, Supporting Information). In total, 16 events in the AARSC could not be paired with another M3+ event reported by any of the 11 individual catalogues (4 of magnitude class A and 12 of magnitude class B):

The occurrence of such events mainly depends on two factors: there exists no complete local seismic catalogue to compare with (e.g. Bosnia-Herzegovina) and the neighbouring national bulletins are incomplete for the region outside their station networks. In the particular case of the Bresse–Graben, the event occurred prior to the installation of the French stations in the region, but was registered by many nearby AASN stations mainly in Germany and Switzerland. In fact, this event is the result of an erroneously location of an unusual strong event (M5.0) near the west coast of France, outside our study region. Our automatic system, however, classified this event as a PL event with an azimuthal GAP of 332°, clearly indicating an unreliable hypocentre solution.

The event in Central Apennines simply documents the difficulties to process swarm events with regular routine procedure. As stated above, with the AARSC processing two M3+ events of the Amatrice sequence have been missed but were reported in the INGV catalogue while one M3+ event reported in AARSC was missed by the INGV.

Apart from these exceptions derived from the pairing with 11 national bulletins for the same time period, we may thus claim that

Downloaded from https://academic.oup.com/gji/article/231/2/921/6609778 by OGS (Istituto Nazionale di Oceanografia e di Geofisica Sperimentale-OGS) Borgo Grotta user on 11 December 2023

the combination of the dense AASN together with our methodological approach leads to the high precision and regionally consistent M3+ AARSC (Fig. 5 and Fig. S13, Supporting Information). In Fig. S14 (Supporting Information), we show three examples of WL event with $M_{Lv} \geq 3$ recorded in the Balkan region that were missing in the respective national catalogue. These events' section clearly show the wavefield corresponding to clear *P* and *S* phases, stressing even more the importance of reinforcing the permanent stations network in the area to homogenize the recordings of an important seismogenic area like the northwestern Dinarides.

4.1 Distribution of seismicity in the GAR

The unprecedented consistency of the new 4-yr catalogue in terms of hypocentre location and magnitude allows discussing the first-order variation in seismicity across this tectonically and dynamically complex region (Fig. 5). In order to relate this short-period seismicity-catalogue with the previous instrumental seismicity reports, we compare the AARSC with the $M \geq 3$ regional seismicity reported by the EPOS-EMSC bulletin for the same period (Fig. 5). In FiSupporting Information), instead, we display the seismicity with $M \geq 3$ reported by the EPOS-EMSC bulletin for the years between 1998 and 2015.

In the western Alps we observe the two well-known seismic arcs (region A, Fig. 5) (e.g. Eva & Solarino 1998; Sue *et al*. 2007; Mathey *et al*. 2021, and references therein). The eastern branch produced more events with $M_{Lv} \geq 3$ compared to the western one, while in the complete AARSC (Fig. 5) both seismic arcs are equally active and their seismicity distribution well corresponds with the 18-yr EPOS-EMSC catalogue (Fig. S15, Supporting Information). Analogue observations could be made for the activity in the NW Alpine foreland (region C, Fig. 5) (e.g. Singer *et al*. 2014; Mader *et al*. 2021 and references therein) and the western part of the eastern Alps (region D, Fig. 5) (e.g. Reiter *et al*. 2018), while the Valais region (region B, Fig. 5) has been showing a slightly increased activity over the recent 4-yr period.

The typical depth distribution of seismicity in the western Alps (Delacou et al. 2004) is shown in Fig. 6, profile B. Within the orogen, the seismicity is constrained to the topmost 25 km of the crust (region A, Fig. 5) with the notable exception of the so-called inner (eastern) seismic arc (Lardeaux et al. 2006) that follows the high-velocity and high-density Ivrea body (see Fig. 6, profile B). The Ivrea body is part of the Adria lithosphere mantle tilted upward and outcropping at the surface at its northern end (Schmid *et al*. 2017; Pistone *et al*. 2020; Scarponi *et al*. 2021, and references therein). While most of the events along this inner seismic arc are confined to the uppermost 25 km, some events may locate as deep as 50 km and thus they are located within the Adriatic uppermost mantle. These findings are in accordance with longer term observations recently summarized and seismo-tectonically interpreted by Eva *et al*. (2020).

The seismicity beneath the Central Alps (regions B–D, Fig. 5) is also confined to the uppermost 22 km of the crustal wedge that reaches a maximum thickness of ∼60 km (Spada *et al*. 2013). In the foreland immediately north of the Alpine front, however, the whole continental crust is seismogenic with deepest events just above the Moho (Deichmann 1992). The difference in depth distribution between the northern foreland and the Alps has been shown to correlate with the stress variation in the European lithosphere caused by the down bending and rollback of the remnant mantle lithosphere slab still attached to Europe between longitude 8E and 11.5E (Singer *et al*. 2014).

The recent M3+ activity in the southern Alps (region E, Fig. 5) and in Friuli (region F, Fig. 5) well corresponds with the longer term catalogue (Fig. S15, Supporting Information). The complete AARSC shows the seismic activity to be localized within a much narrower belt roughly following the southern limits of the orogen and extending toward WSW into the Po plain (Fig. 5, see also Jozi Najafabadi *et al*. 2021; Verwater *et al*. 2021). Interesting enough, the AARSC (Fig. 5) shows four M_{Lv} 2+ events perfectly aligned along the Periadriatic fault (region PF, Figs 4 and 5) just N of Friuli (region F, Fig. 5) where no M3+ has been reported before (Fig. S15, Supporting Information). Nonetheless, recent tectonic activity along the Periadriatic and the seismically more active Fella-Sava fault systems has been discussed by Bartel *et al*. (2014a,b).

Within the northern Apennines portion included in the GAR (regions G–H–I, Fig. 5), the northern limits of the extensive seismicity during both the 4- and the 18-yr periods well correlates with the Apennines front situated within the unconsolidated sediment of the Po-Plain (I). Between the marked regions (G–H–I) there are small seismicity divisions documented in the EMSC catalogue (Fig. 5 and Fig. S15, Supporting Information) that denote examples of the intermittent Apennines seismicity typically showing clustered sequences related to the locally varying active tectonic regimes (extensional and compressional) and the segmented reactivation of low-angle faults (Frepoli & Amato 1997; Collettini & Barchi 2002, and reference therein).

One of the largest historical events of northern Italy was the ∼6.5 M_w Lunigiana–Garfagnana earthquake of 1920 (Rovida *et al*. 2016). In the same region of the Po-Plain occurred the recently recorded important seismic sequence (Scognamiglio *et al*. 2012). This subregion indeed represents a highly hazardous and seismic risk area. Severe site effects may occur from even a medium size event due to the amplification by wave reverberations in unconsolidated sediments (van Ede *et al*. 2020). The seismicity in the northern Apennines is mostly shallow and confined to the top 20 km of the crust with the exception of some events occurring in the deep Adria crust (Fig. 6a). The A-profile depicts a representative cross section across the northern Apennines documenting the rollback dynamics of the down bending Adria lithosphere into the SW vergent subduction zone (Molli *et al*. 2010; Chiarabba *et al*. 2014; D'Acquisto *et al*. 2020). The same profile indeed shows that a large part of the Apennines is actually underlined by Tyrrhenian Moho and the NE part of the Apennines front denotes thrusting and normal faulting entirely within Adriatic crustal units. In addition, the structure within the Po plain basin on Apennines side and the Venetian Friuli basin on the southern Alps side has been well documented by industrial reflection seismic. On the base of this data, Carminati & Doglioni (2012, fig 24) associate this structure to the current thrusting of upper crustal slivers from SW in Apennines and from NE in Friuli.

The seismicity distributions in the region N and E of Trieste as evidenced by the profiles A and C in Fig. 6, and Fig. 4 documents the tectonic complexity of the area between the southern/eastern Alps and the northern Dinarides (e.g. Laubscher 1971; Castellarin *et al*. 2006; Kissling *et al*. 2006; Ustaszewski *et al*. 2008, Handy *et al*. 2010).

The AARSC also well delineates the two branches of seismicity that follow the main two active fault systems in the northern Balkan region (region DFS-SKF, Fig. 5). The eastern and western seismicity branches are generally associated with the Adria subduction and northwestern Dinarides orogeny processes (Horváth & Cloetingh

Downloaded from https://academic.oup.com/gji/article/231/2/921/6609778 by OGS (Istituto Nazionale di Oceanografia e di Geofisica Sperimentale-OGS) Borgo Grotta user on 11 December 2023

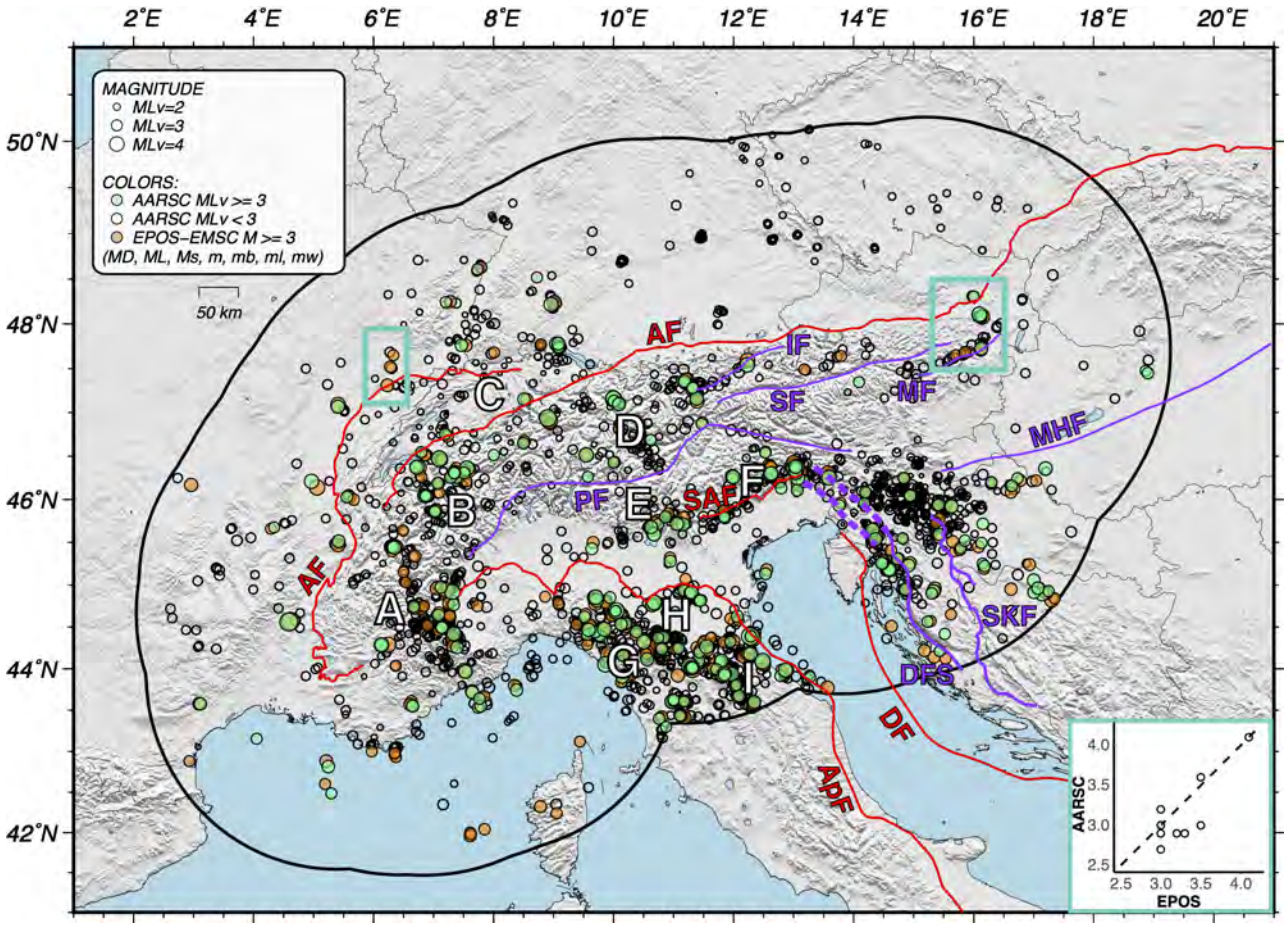

Figure 5: Epicentres map comparing the seismicity reported by the AARSC and the EMSC (provided by EPOS) for the time period 2016 January 1–2019 December 31. Filled orange circles represent the events with $M \geq 3$ extracted from EPOS-EMSC; filled green circles represent the WL events with $M_{Lv} \geq 3$ extracted from the AARSC; empty circles represent the WL events with M < 3 extracted from the AARSC. Orogenic fronts (red lines) and major tectonic lineaments (purple lines) simplified from Schmid *et al*. (2004, 2008), Handy *et al*. (2010) and; Kästle *et al*. (2020) (see Fig. 4 for details). For the discussion of seismicity in selected areas of interest (marked by white letters A–I) and selected fault segments see the text. This figure clearly documents the close similarity in the epicentral distributions resulting from our semi-automatic processing with the manually revised locations provided by the EMSC. Missing green circles where orange circles are present (light-blue squares), do not necessarily mean missed events, but rather a pairing of those EPOS-EMSC events with a lower magnitude event from AARSC (lower right box). See the main text for details.

1996; Pamić *et al*. 1998; Poljak *et al*. 2000; Brückl *et al*. 2010). Together with the Apennines, these regions are of highest seismic activity in the GAR.

In the following, we briefly describe a few prominent examples of seismically active faults in the GAR. The Mur-Mürztal fault system (region MF, Figs 4 and 5) has long been recognized as a source region of potential seismic hazard (Lenhardt *et al*. 2007). During the 2016–2019 period, it has been active along its ∼100 km fault length although only one event occurred with a magnitude larger than M_{Lv} 3. The eastern part of the Inntal fault system has been equally active (region IF, Figs 4 and 5, Reiter *et al*. 2003; Jozi Najafabadi *et al*. 2021). These activities observed during the 4-yr period of AARSC occur on faults that belong to an extensive fault system within the eastern Alps. These are usually associated to the regional lateral extrusion tectonics (e.g. Ratschbacher *et al*. 1991; Ustaszewski *et al*. 2008; Handy *et al*. 2010, 2015). However, its most prominent member, the SEMP fault (region SF, Figs 4 and 5) has not been seismically active with events of magnitude larger than M_{Lv} 2.4.

Overall, the precise and consistent event locations allow to better define and constrain both major and minor active tectonic lineaments within the GAR. In particular, some events locally show really good match with tectonic lineaments in highly seismically active regions (e.g. region A, H IF, MF, DFS in Fig. 5).

4.2 Magnitudes comparison across the GAR

For the AARSC, we used a uniform M_{Lv} magnitude scale for our calculations providing a consistent magnitude estimation across the GAR (see Section 3.6). In fact, all of the 11 national and local agencies operating inside the GAR adopt different magnitude scales to assess the event's seismic energy release. The magnitude scale heterogeneities can be best observed by comparing the magnitudes of the paired events for the agencies individually with the AARSC. The statistics reported in all the Fig. 7 and Fig. S16 (Supporting Information) panels represent the mean value and standard deviation of the magnitude residuals distribution for the paired events and

Downloaded from https://academic.oup.com/gji/article/231/2/921/6609778 by OGS (Istituto Nazionale di Oceanografia e di Geofisica Sperimentale-OGS) Borgo Grotta user on 11 December 2023

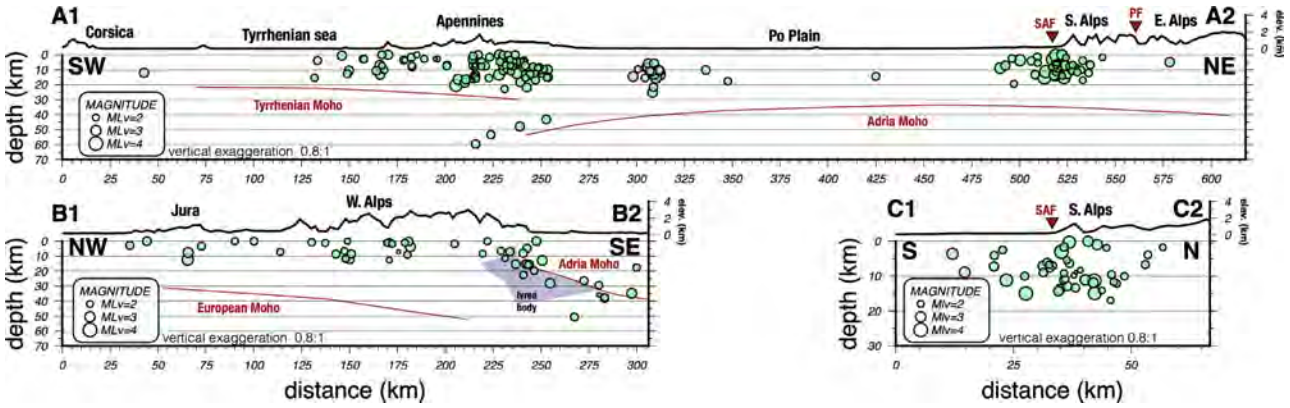

Figure 6: AARSC WL hypocentre distributions along three profiles A1–A2, B1–B2 and C1–C2 (for geographical locations, see Fig. 4). For reference, the Moho topography following Spada *et al*. (2013, solid red line) is shown. Profile (A1–A2) crosses both the northern Apennines and the southern Alpine tectonic fronts and regions of relative high seismicity. Note the pronounced Moho offset beneath the northern Apennines front including four deep-crustal events evidencing the subduction of Adria plate beneath the Tyrrhenian plate. Profile (B1–B2) follows the EE′ transect of Diehl *et al*. (2009c). This profile documents the generally shallow crustal seismicity of the northwestern Alpine foreland and within most parts of the western Alps, while the seismicity in the so-called inner seismic arc (Eva & Solarino 1998) and related to the Ivrea body (Schmid *et al*. 2017) reaches down to depth of 50 km. Note the very large vertical offset between the deep European Moho and the Adria Moho marking the top of the Ivrea body that outcrops further North. Profile (C1–C2) represents a short transect perpendicular to the southern Alps orogenic front in the vicinity of the junction with the Dinarides documenting complex thrusting tectonics. All three sections include events in a band of 25 km on either side of the profile (see grey bar around profiles in Fig. 4). SAF and PF respectively mark the locations of the southern Alpine front and the Periadriatic fault intersections with the profiles.

provide a solid, quantitative measurement of the agencies' magnitude scales shift. The four examples in Fig. 7 evidence some possible scenarios when comparing the different scaling coming from different agencies. The manuscript's supplementary material additionally contains five of the remaining agencies pairing comparisons (Fig. S16, Supporting Information). Unfortunately for ASCR (Czech Republic) and ESISAS (Slovakia) no meaningful statistics are available due to only 3 and 1 M3+ event pairs respectively. This provides the chance to compare a uniform magnitude scale against those of the 11 different networks. Previously, this was only possible between overlapping competence areas and for a small subset of data (e.g. Fig. S2, Supporting Information).

In Fig. 7(a), a strong correlation between AARSC-M_{Lv} and SED-M_{Lh} is clear, apart from a single outlier related to a doubled paired event (e.g. one event of AARSC pairs with two different ones reported by the SED).

Although similar, the linear fit between INGV and AARSC magnitude tend to deviate from the 1:1 relation towards higher magnitudes, thus indicating a general magnitudes overestimation of AARSC for $M_{\mathrm{Lv}} \geq 3.5$ (Fig. 7b). The same behaviour, although in opposite direction, occurs when comparing the local magnitudes of AARSC together with one of RESIF (Fig. S16d, Supporting Information). Here, the deviation towards higher magnitudes ($> 3.5\ M_{\mathrm{Lv}}$) indicates an underestimation tendency for AARSC magnitudes. The pairing between OGS and AARSC, instead, shows a deviation from the 1:1 relation both at high and low magnitudes values. This indicates a trend of underestimation of lower magnitudes and overestimation at higher magnitudes of the AARSC events. The last case scenario shows a shift between the magnitudes calculated by ARSO and the ones contained in AARSC, thus evidencing a consistent overestimation for the entire magnitude range contained in the AARSC (Fig. 7d).

The nature of these different behaviours mainly depends on two factors (or even a combination of both): (i) the use of different attenuation functions and *ad-hoc* station's site effect corrections, (ii) a mixed report of magnitudes scales inside the same bulletin (e.g. local and moment magnitudes).

4.3 Minimum 1-D *P*-wave velocity model and station delays for the GAR

Prior to the final production scheme (Fig. 2), we selected a subset of 2595 events based on a preliminary VELEST run, aimed at detecting the most reliable hypocentres. With a total number of 103 844 *P*-observations (∼40 observations per event on average) recorded between 2016 and 2019, we calculated a new minimum 1-D *P*-wave velocity model and corresponding station delays for the GAR (Fig. 8) following the method described in Kissling *et al*. (1994).

A minimum 1-D model with station delays does not simply represent an inversion's mathematical minimum. In fact, the coupled hypocentre-velocity model inversions might yield ambiguous solutions as there might be a few local minima. The solution of choice provides a 1-D average crustal velocity model reasonably well corresponding with *a priori* information obtained by refraction seismic profiling and station delays that regionally correspond with the near-surface geology (Kissling 1988). Considering the large size of the GAR completely and uniformly covered by the AASN, however, the station delays in the more peripheral regions will also be affected by the strongly variable Moho topography (Spada *et al*. 2013) since the larger magnitude events will be well observed to greater distances by *Pn* arrivals (Fig. 8a). These first arrivals usually exhibit a rather uniform waveform and thus are well observed and identified by the ADAPT-JHD-VELEST system but, due to the wave travel path, the traveltime includes effects both of the Moho topography and of the normal shallow crustal structure (e.g. sedimentary basin fill).

For the GAR-wide minimum 1-D model we choose the reference station IV.MABI (INGV permanent network) located at latitude 46.05°N and longitude 10.51°E near the centre of the region (marked by a black star in Fig. 8a) in the southern Alps with a reported Moho depth of about 38 km (Spada *et al*. 2013). The outermost grey profiles in Fig. 8(b) represent the input models for our minimum 1-D *P*-wave velocity model stability test (Quintero & Kissling 2001).

In general, the station delays show a strong regional consistency except for those stations listed with zero delay as a consequence

Downloaded from https://academic.oup.com/gji/article/231/2/921/6609778 by OGS (Istituto Nazionale di Oceanografia e di Geofisica Sperimentale-OGS) Borgo Grotta user on 11 December 2023

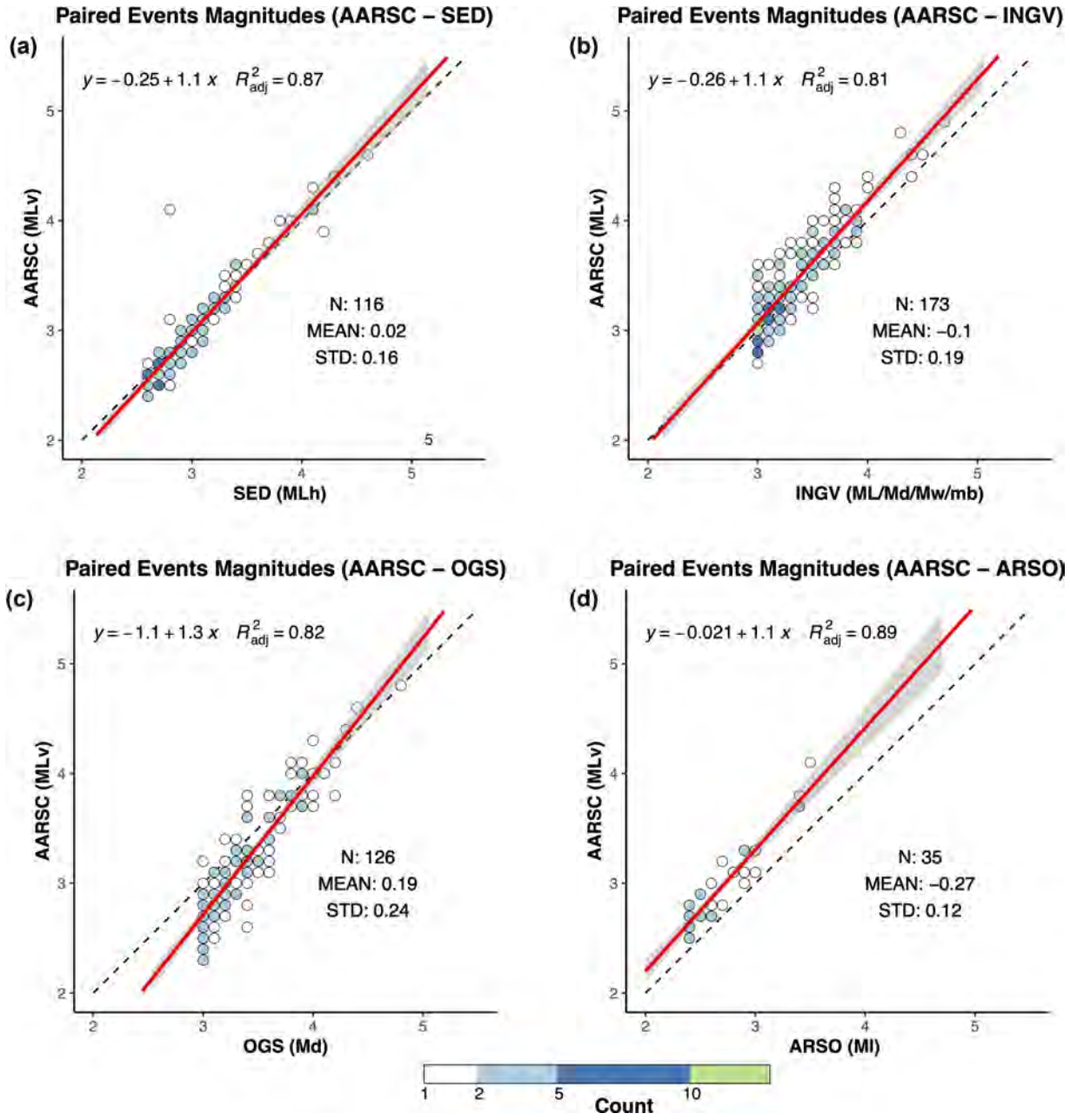

Figure 7: Events magnitudes comparison between the AARSC and individual catalogues from national and local agencies. This figure compares only events that could be paired between the individual agency catalogues and the AARSC. We here show only 4 of the 11 seismic bulletins analysed: the (a) SED (Switzerland), (b) INGV and (c) OGS (Italy), and the (d) ARSO (Slovenia) as examples of possible scenarios when pursuing catalogue merging in the GAR. These scenarios may vary from a consistent relative underestimation of magnitude by the local observatory (d), to a relative overestimation at lower magnitude combined with an underestimation at higher magnitude (c) and to a fair to good correlation of magnitudes with higher (b) or lower (a) noise level. For each panel we provide the principal statistical information to quantitatively describe the differences among the different magnitude scaling. These include the regression line equation, the adjusted *R*-squared model accuracy, the mean and standard deviations of paired magnitude residuals, and the number of pairs in the data sets. The dashed black line represents the 1:1 relation. This figure clearly evidences the heterogeneities among the individual agencies operating in GAR.

of insufficient data (e.g. less than 20 observations). Since the vast majority of the seismic events occur in the top 20 km of the crust, the station delays prominently reflect the regional crustal velocities in combination with Moho topography. As expected, the station delays within the Alps relative to the reference station in the southern Alps are relatively small. Early arrivals within the Alps are confined to the region of outcropping igneous basement rocks along the central axis of the orogen while slightly delayed arrivals occur along the northern Prealps. These latter are dominated by thick sedimentary nappes including sub-alpine Molasse overthrusting the basement rocks. The Molasse sedimentary basin is characterized by moderately delayed arrivals increasing in amplitude from W to E and nicely corresponding with width and depth of the basin. The station delays in the northern Alpine foreland beyond the Molasse basin show the combined effects of the local crustal velocities and the Moho topography. In fact, the arrivals from distant hypocentres are almost exclusively *Pn* phases (critically refracted at Moho) that arrive early. This because the Moho shallows significantly from

Downloaded from https://academic.oup.com/gji/article/231/2/921/6609778 by OGS (Istituto Nazionale di Oceanografia e di Geofisica Sperimentale-OGS) Borgo Grotta user on 11 December 2023

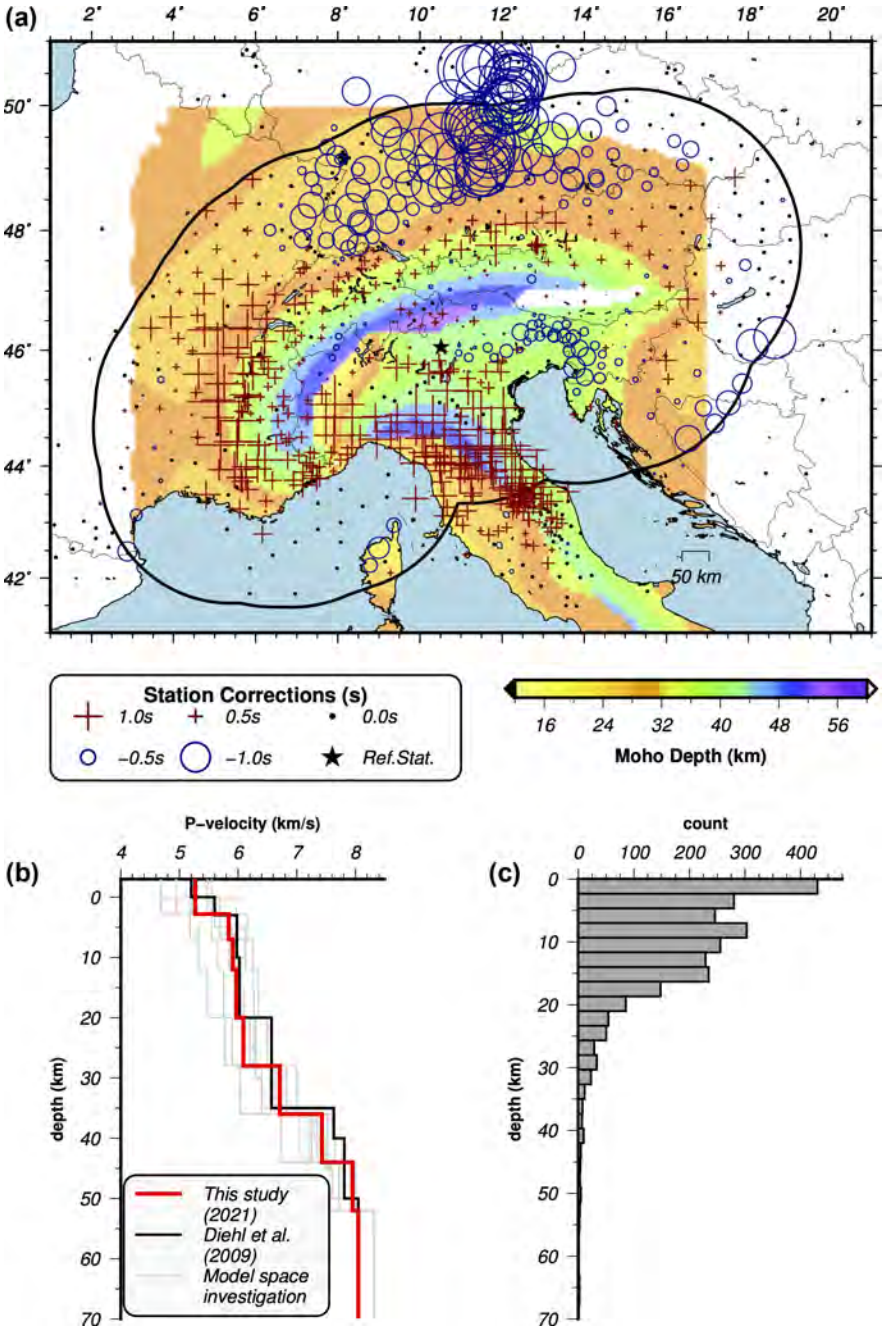

Figure 8: Minimum 1-D *P*-wave velocity model and corresponding station delays for the GAR. (a) Station delays (both permanent and temporary stations with at least 20 observations are shown) used for traveltimes prediction and event relocation superimposed on the Moho map (Spada *et al*. 2013). Positive delays (red crosses) indicate late arrivals and negative delays (blue circles) indicate early arrivals compared to the reference station. Symbol size corresponds to the amplitude of time delay. (b) 1-D *P* velocity–depth profiles. The most recently published 1-D *P*-wave velocity model for the area (Diehl *et al*. 2009a) is shown by a solid black line. The light grey lines represent the various initial models used to investigate the model space to clarify convergence to a meaningful minimum 1-D velocity model. The solid red line represents the new 1-D *P*-wave velocity model for the GAR. (c) Hypocentre's depth distribution of the events used in the minimum 1-D model calculations.

about 50 km beneath the Alps to a minimum of 24 km beneath the southern Rhine Graben and the Swabian Jura (Fig. 6a). Thus, the *Pn* phases are all following the Moho uphill direction leading to early arrivals independently of the hypocentre depth. East of longitude 6°E early arrivals dominate as a consequence of the relatively high middle and upper crustal velocities. In addition, the absence of thick layers of unconsolidated sediments at the surface and of the relatively shallow Moho reinforce such behaviour (as mentioned above).

The moderate to pronounced delayed arrivals West of longitude 6° E and South of 47° N relate to regular upper crustal velocities, to pronounced near-surface low velocities. The locally thick unconsolidated sediments of the Bresse and Rhone Graben systems and the slightly deeper Moho (Fig. 6a) are likely the reason of these delays. The pronounced late arrivals at all stations in the Italian peninsula results from the thick sedimentary rock layers either consolidated within the Apennines or unconsolidated sediments in the Po plain.

Downloaded from https://academic.oup.com/gji/article/231/2/921/6609778 by OGS (Istituto Nazionale di Oceanografia e di Geofisica Sperimentale-OGS) Borgo Grotta user on 11 December 2023

Table 1: Minimum 1-D *P*-wave velocity model layering and corresponding velocities.

Depth (km)	Velocity (km s^{-1})
−3.50	5.27
2.80	5.84
7.00	5.91
12.00	5.97
20.00	6.09
28.00	6.71
36.00	7.43
44.00	7.95
52.00	8.05
90.00	8.15

The layering and related *P*-wave velocities of the minimum 1-D model are reported in Table 1.

5 DISCUSSION

The semi-automatic workflow and the algorithms here explained could potentially be applied to any other places in the world. Although better suitable to investigate regional seismicity, no limits exist on the scalability of the problem. The non-trivial procedure is certainly the tuning of the ADAPT-JHD individual sections. While the production of a preliminary catalogue (step 1) can be achieved with other software (i.e. EW), careful attention must be given to the event filtering stage (step 2) and to the re-picking stages (steps 3 and 5). For the event filtering scheme (see Text T3 in the Supporting Information) a possible refinement of the given filtering thresholds could be necessary. For ADAPT itself, is recommended to start with a reference data set that is representative of the region investigated. Once manually picked with a consistent error assessment, those picks can be used as a ground truth to tune the individual pickers and the phase identification stage. As explained in Section 3, the ADAPT library can be used with less or different picker combinations. The same applies for the number of slicing windows and customizable tests for phase identification and phase recognition. These decisions may vary (even strongly) between one case study and another. The reader is referred to Bagagli (2022) for details on tuning and best-usage recommendations for both ADAPT and VELEST software.

Our ADAPT-JHD-VELEST workflow's approach for picking and locations is focused on *P*-wave first arrival only. This choice is based on the following reasons. The automatic picking of *S*-phases is a renowned difficult task given all the hidden pitfalls included (e.g. Cichowicz 1993; Diehl *et al*. 2009b). Unreliable phase identification and higher risk of surface wave picking may undermine the final picks data set consistency. On the other hand, it is also true that the correct identification and recognition of seismic *P*-wave first arrivals is not a straightforward task. In this work, with our multistep procedure, we managed to get these problems largely solved for the *P* waves. In general, it is true that event locations would benefit from the usage of *S*-phases as well. Nonetheless, to achieve the same high quality and consistency as our *P*-data set would not only have required the calculation of a minimum 1-D model with appropriate station delays for *S* waves prediction but also to apply a procedure for correctly identifying *Sg* and *Sn* phases. Unfortunately, the latter, in particular for *Sn* phases, is beyond the possibility of the ADAPT-JHD-VELEST structure and we do not know of another automated software that currently provides a solution to this task.

On the other hand, because WL events are intrinsically well constrained in their final epicentres, the detection and utilization of *S* phases for event location would have helped primarily the PL events. An example of such a potential benefit is given by the AARSC event in the Bresse–Graben, which is associated with an erroneous location of a bigger event (*M*5.0) at the west coast of France. In this case, the picking of *S* phases would have been beneficial for the correct location. Assessing the *S*–*P* time from the waveforms of this event clearly identifies it to be outside of the GAR.

The comparison between the M_{Lv} 3+ AARSC and the M3+ regional catalogue provided by EPOS-EMSC for the time period 2016–2019 (Fig. 5) documents a largely similar seismicity across the GAR. The epicentre and magnitude comparison suggests that the quality of the AARSC semi-automatic solution is similar to the one reported in the manually revised EPOS-EMSC bulletin. Furthermore, the successful M3+ event-by-event pairing of the AARSC with the catalogues from the 11 national observatories documents the importance of having an automatic system for observatory routine processing of such a large station network to obtain uniform, consistent and less error-prone reports. However, the 4-yr time period is not long enough to document all potentially active regions in the GAR. In fact, the different area's seismic activity ratio did not allow to observe the complete magnitude distributions of individual subregions. Nonetheless, considering the consistent and high-precision hypocentre locations in the AARSC across the whole GAR, we can comparatively analyse in more detail several seismically active sub-regions of the Alps (e.g. subregions A–F, Fig. 5).

The regionally consistent event pairing allows us to quantitatively assess the effects of the various magnitude scales applied in those catalogues (Fig. 7). It also documents that, with a fully automated processing system, the AARSC would have missed 8 events (fully described in Text T4 in the Supporting Information). For the purpose of improving the system it is worth noting that seven out of these eight cases depend on detection failures of our SC3 automatic system (step 1, Fig. 2). Thus, we may conclude for large station arrays the new fully automated method of ADAPT-JHD-VELEST performs very well. In fact, thanks to the high spatial density of the AASN we eventually detected an additional 16 M_{Lv} 3+ events compared to the reports by the national observatories, including the above-mentioned mislocation in the Bresse–Graben of a stronger event at the west coast of France. We show three of these additional successful detection examples in Fig. S14 (Supporting Information), where one could appreciate the wave-trail of both *P* and *S* waves approaching the array. Indeed, most of these events (14) were detected in the northern Balkan region (Croatia and Bosnia–Herzegovina) suggesting that the permanent stations coverage could be improved to detect all the M3+ events in the region (Fig. S13, Supporting Information). This is indeed one of the main reasons for follow-up projects like AdriaArray.

5.1 Frequency–magnitude distributions

Magnitude scales heterogeneities remain a major issue when merging routine national and regional seismicity-catalogues. In Figs 5 and 7, and Fig. S16 (Supporting Information), we clearly document the difficulties to correctly match events according to hypocentre locations, origin times and magnitudes by comparing our catalogue against the national ones across the GAR. In our AARSC we use a uniform local magnitude calculation (M_{Lv}) across the entire GAR, allowing us to consistently compare the seismic energy released by the events across this tectonically complex region. Even though

Downloaded from https://academic.oup.com/gji/article/231/2/921/6609778 by OGS (Istituto Nazionale di Oceanografia e di Geofisica Sperimentale-OGS) Borgo Grotta user on 11 December 2023

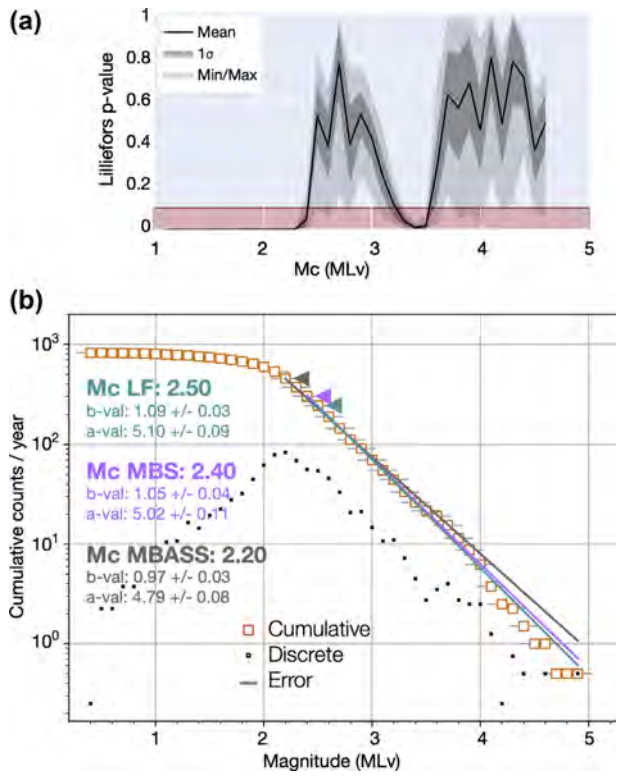

Figure 9: FMD of the entire AARSC 2016–2019. In the upper panel (a), we show the LF tests (Lilliefors 1967; Herrmann & Marzocchi 2020) for the magnitude of completeness (M_c) determination. The significance level α used for null hypothesis testing is highlighted in red in (a): it divides the possible interval values for the exponentiality fit. Panel (b) reports the actual discrete (black squares) and cumulative (orange squares) FMD of the entire catalogue. For the FMD we report the analysis 3 well-based algorithm for M_c and *a*/*b*-values estimation: LF (Lilliefors 1967; Herrmann & Marzocchi 2020), MBASS (Amorese 2007) and MBS (Cao & Gao 2002; Woessner & Wiemer 2005). See text for details.

the AARSC spans only a 4-yr period, we try to obtain a first order insight into the frequency–magnitude distribution (here after FMD).Several methods have been proposed in the past to interpret the FMD in terms of magnitude of completeness (M_c) and *a*- and *b*-values. Among these, four catalogue-based approaches are extensively used in literature: the maximum-curvature method (MC, Wyss *et al*. 1999; Wiemer & Wyss 2000), the method to calculate M_c by assessing *b*-value stability (MBS, Cao & Gao 2002; Woessner & Wiemer 2005), the median-based analysis of the segment slope (MBASS, Amorese 2007) and the canonical Lilliefors test (LF, Lilliefors 1967, Herrmann & Marzocchi 2020). The MC method simply defines the M_c as the statistical *mode* of the discrete FD (black squares in Fig. 9b and Fig. S18, Supporting Information) plus a correction factor (Wiemer & Wyss 2000). Although analysing differently the FMD distributions properties, the MBS, MBASS and LF methods are statistically more robust. The MBASS analyse the stability of the *b*-value by checking the slope variation between adjacent magnitude bins, and declare the final M_c when the highest discontinuity magnitude is reached (Amorese 2007, fig. 2). Such a method is very robust against possible kinks in the FMD distribution, and tends to underestimate the true M_c (Amorese 2007; Mignan & Woessner 2012). The MBS method on the contrary, calculates *b*-values as a function of cut-off magnitudes from the maximum magnitude (Cao & Gao 2002; Shi & Bolt 1982). When the difference between the *b*-values in two neighbouring steps is less than a fixed threshold, that value represents the final result (Cao & Gao 2002; Woessner & Wiemer 2005; Mignan & Woessner 2012). Thus, the MBS method tries to fit the entire distribution's GR-slope rather than checking the individual variation among individual bins. Moreover, this latest approach provides more conservative estimates in case of a more curved FMD's shape, and so it tends to overestimate the final M_c (e.g. Fig. S18d, Supporting Information, Mignan 2012; Mignan & Woessner 2012). For an exhaustive review of the two methods MBASS and MBS, the reader is referred to Mignan & Woessner (2012), and references therein.

The approach of LF method for M_c calculation is to define the probability of exponentiality of an FMD distribution at subsequent magnitude cut-offs based on a goodness-of-fit method (Fig. 9a, and Fig. S18a, c, e and g, Supporting Information). This method has been already used in the past, often termed 'modified KS test' referring to either Stephens (1974) or Pearson & Hartley (1972). The associated *a*- and *b*-values are calculated with a bias-free maximum-likelihood regression (Tinti & Mulargia 1987; Marzocchi & Sandri 2003) fixing the M_c to the one previously estimated. By using the ensemble of the three methods MBS, MBASS and LF, we aim to obtain more information about the nature of the distributions itself.

In Fig. 9(a), we observe a drop of the distribution exponentiality fit (LF test) reflecting in a slope-break around 3.5 M_{Lv} in Fig. 9(b). Such behaviour is common when analysing ML catalogue-based FMD. The main reasoning behind this are the spatio-temporal inhomogeneities of the catalogue and the local magnitude scale definition itself. The slope-break in scale around M_{Lv} 2–4 may also depend to the anelastic attenuation in the medium acting as a low-pass filter (Bethmann *et al*. 2011; Munafò *et al*. 2016; Deichmann 2017; Herrmann & Marzocchi 2020).

Finally, using different statistical approaches in our calculations, we can observe different M_c values ranging between 2.2 and 2.5 M_{Lv}. We decide to set our final AARSC-M_c to 2.4 M_{Lv} with the associated *b*-value of 1.05, based on the MBS results that fall within the upper and low boundaries of the possible M_c range.

The *b*-value of 1.05 might be related to the short analysis period (4 yr), as we potentially miss relatively rarely occurring larger magnitude ($M_{Lv} > 4$) activity. Consequently, this increases the relative weights of the lower magnitudes in the maximum-likelihood regression fit. An increased number of smaller earthquakes compared to larger ones may also suggest a preferred energy-dissipation trend toward small earthquakes (Staudenmaier *et al*. 2019, and reference therein) in the GAR at least during these 4 yr.

To further investigate whether different behaviour occurs in specific seismogenic zones, we split the catalogue into 4 subregions (Fig. S17, Supporting Information): (i) the northern Apennines, (ii) the Alps, (iii) the Alpine foreland and (iv) the northwestern Dinarides. We report all these results in Fig. S18 (Supporting Information).

The northern Apennines shows a consistent M_c and *b*-values for all methods used and a stable exponentiality fit at a wide range of magnitude cut-offs as evidenced by the LF test (Fig. S18e, Supporting Information). The GR regression of the FMD distribution is remarkably stable, although showing a slightly higher *b*-value than the GAR. On the contrary, all the Alpine region is fully included in our analysis, and its seismicity shows a more complete distribution. The *b*-value associated to this region is the closest to 1 among all subregions and reports similar behaviour like the entire AARSC-FMD (Fig. S18b, Supporting Information). However, the Alpine foreland remains hard to interpret due to the relatively few events located, and the shape of its FMD is heavily biased by the single 4.9 M_{Lv} event present (Fig. S18h, Supporting Information).

Downloaded from https://academic.oup.com/gji/article/231/2/921/6609778 by OGS (Istituto Nazionale di Oceanografia e di Geofisica Sperimentale-OGS) Borgo Grotta user on 11 December 2023

The northwestern Dinarides show FMD shapes (Fig. S18d, Supporting Information) similar to the one reported in Mignan (2012, fig 5b). Such distributions usually indicate regional FMD with large M_c variation due to strong spatio-temporal heterogeneities in stations distributions deriving, for example, from the superimposition of regional and temporary networks (Mignan 2012). This could as well reflect the general problems of stations metadata completeness and data quality for the subregion during the experiment (Fig. S3, Supporting Information).

Our results are only an initial and partial analysis of the magnitude distribution of our catalogue. Any further interpretation of the M_c and *a*-, *b*-values at this stage would be merely speculation. In addition, such catalogue-based methods must always be interpreted with caution by knowing the true nature of the data (Marzocchi & Sandri 2003; Deichmann 2017; Herrmann & Marzocchi 2020). An exhaustive magnitude study for both the entire GAR and the individual seismogenic subregions is a bold and careful task that is beyond the scope of this study. With the newly updated and detailed regional attenuation functions (Bindi *et al*. 2019), one could refine the local and moment magnitudes and improve their interpretations. Additionally, the derivation of a new, regional M_{Lv}–M_w fitting model would also greatly improve the magnitude analysis of the GAR.

Furthermore, for a more solid, complete and exhaustive interpretation of these magnitudes one would need a much longer period of analysis (Giardini *et al*. 1999; Woessner *et al*. 2005, 2015; Giardini *et al*. 2018). Such a long-term seismic catalogue with the same consistency and precision like the AARSC, could be achieved by using the minimum 1-D model and station delays obtained from this study for application to previous catalogues established by the permanent networks.

5.2 Establishing a long-term seismicity-catalogue for the GAR

Several national and regional seismic networks in the GAR date back to the early 1970s with limited number of stations. For most of the stations, however, waveforms are only available since the mid-1990s and calculations of event catalogues by merging of arrival times for events collected by different observatories remains a difficult task and sometimes leads to ambiguous results and mismatches (e.g. Blundell *et al*. 1992; Solarino *et al*. 1997). A consistent instrumental seismic catalogue of M3+ events for the GAR could possibly be compiled for the past two decades if the registered events waveforms were available. A minimum 1-D model and stations delays is a prerequisite for merging a consistent catalogue and the ones calculated for the GAR (Fig. 8). They represent the ideal tool to link past and present seismicity because the results do refer to all permanent stations operated by the 11 individual observatories (Fig. S1, Supporting Information) in addition to the AASN stations.

Of course, with a series of minimum 1-D models combined and appropriate station delays for the GAR, the local crustal structure could be better approximated and, hence, locally we could achieve higher precision hypocentre locations (e.g. Husen *et al*. 2011). Furthermore, with a series of local minimum 1-D models one would be able, for each model, to choose a locally more appropriate and useful reference station than the one in the southern Alps chosen for the GAR and this might allow to illuminate more details of the local velocity variations by updated stations delays. For the purpose of establishing a catalogue with consistently precise hypocentre locations across the GAR, however, a single minimum 1-D model provides the optimal reference data set to recognize corresponding events reported by nearly a dozen different observatories. Furthermore, this single minimum 1-D model with the appropriate set of station delays not only for the AASN but for all permanent seismic stations in the GAR are key tools to identify, filter and merge information of events reported in the catalogues from times before (and also after) the AlpArray experiment. An obviously challenging and important task for seismic hazard assessment is the full reprocessing of the long-term seismicity stations waveforms available from the various seismic observatories with the method presented in this study (Fig. 2). Consider that events located in the periphery of one network are obviously close but still outside the networks of the neighbouring observatories leading to PL events (azimuthal GAP $\geq 180^\circ$). The larger magnitude events will undoubtedly be registered and often be reported by several networks. Nonetheless, the hypocentre locations and the magnitudes reported will likely differ significantly. Precisely for such cases, a uniform minimum 1-D model for the whole region with appropriate station delays for all permanent seismic stations operated by the 11 seismic observatories is of particular relevance to facilitate the catalogue merging process.

6 CONCLUSIONS

In this work, we present a new highly consistent and precise seismic catalogue for the GAR. The catalogue covers a 4-yr time period from 2016 January 1 up to 2019 December 31 and it is compiled in the framework of the European collaborative project AlpArray (www.alparray.ethz.ch). All the processed data are recorded by the AASN, a uniform densely spaced station array composed of the 561 BB stations by 11 national permanent seismic networks and 288 temporary BB seismic stations. It is additionally complemented by permanent short-period sensor and accelerometer stations leading to a total of 1103 seismic stations and collecting ∼50 TB of data.

For the processing of such a large amount of data, we developed a new fully automatic, multistep procedure for regional seismic catalogue compilation. This method involves the use of well based standard seismic-processing software and algorithms (Fig. 2): the SC3 system, the ADAPT multi-picking library, and the VELEST software.

The final AARSC contains 3293 relocated earthquakes with magnitude ranging 0.4–4.9 M_{Lv}. The classification of the data set is divided as follows: 2869 WL ($N\_P_{obs} \geq 7$ and GAP $< 180^\circ$), 387 PL (GAP $\geq 180^\circ$ or $4 < N\_P_{obs} < 7$) and 37 VPL ($N\_P_{obs} = 4$) events, of which 1145 have magnitude class A and 2144 magnitude class B. Four events (2 PL and 2 VPL) have no magnitude because no station magnitude observations are left after the quality filtering (see Section 3.6). We calculated a uniform local magnitude (M_{Lv}) across the entire GAR for all events in the AARSC and analysed the FMD distribution with three well-known statistical algorithms (MBASS, MBS and LF) evidencing a consistent and stable GR regression over the M_{Lv} scale. The AARSC is complete down to 2.4 M_{Lv}. Furthermore, based on paring AARSC with 11 national observatories M3+ seismic bulletins for the same time period, the catalogue is regionally consistent down to 3.0 M_{Lv}. The uniform magnitude distribution allowed us to compare the AARSC scaling against the one adopted by the national agencies (Fig. 7 and Fig. S16, Supporting Information), evidencing similarities and differences related to different amplitude correction functions.

With just a few exceptions requiring manual controlling, the semi-automated ADAPT-JHD-VELEST method performs well, resulting in high-precision hypocentre locations (location errors in

Downloaded from https://academic.oup.com/gji/article/231/2/921/6609778 by OGS (Istituto Nazionale di Oceanografia e di Geofisica Sperimentale-OGS) Borgo Grotta user on 11 December 2023

95 per cent of WL events for epicentre are ±0.7 km and for the hypocentre depth are ±2 km). These results document the ADAPT-JHD-VELEST automated procedure to be a reliable and efficient tool for seismic catalogue processing, in particular regarding the single observation and event filtering. The presented 4-yr catalogue of the GAR resulting from semi-automated processing nicely correlates with the regional manually revised bulletin of EPOS-EMSC (Fig. 5). It also well delineates several major and minor seismically active tectonic lineaments, including orogen fronts throughout the study region. The AARSC internal consistency and high-precision documents the importance of automatic methods to side humans in seismic observatories duties.

To achieve the same consistency and uniformity in establishing a longer term seismicity-catalogue, one should take advantage of the minimum 1-D *P*-wave velocity model for the GAR and appropriate stations delays obtained in this study. The minimum 1-D model is only representing the large-scale *P*-wave velocity average lithosphere (mainly crustal), because of the substantial extent, the significant Moho topography and strong crustal heterogeneities of the investigated area. On the other hand, the station delays regionally well define the main features of the upper crustal *P*-velocity structure in the GAR. We hope that the seismological community may benefit from these deliverables and that the consistency and precision of the AARSC will help further seismic studies in the GAR, including (but not limited to) local earthquake seismic tomography.

ACKNOWLEDGMENTS

Three anonymous reviewers are acknowledged for the constructive criticisms that greatly helped improving the quality of the manuscript. We would like to thank John Clinton, Luca Scarabello, Philip Käestli, Roman Racine and Frédérick Massin for their invaluable technical support. The AlpArray-Switzerland project is funded by the Swiss-AlpArray SINERGIA project CRSII2_154434/1 by Swiss National Science Foundation (SNSF). We are also thankful to all the agencies referee that shared their catalogue via personal communication so that this manuscript could benefit from those comparison: Jurij Pahor and Mladen Živčić (ARSO), Dr Thomas Plenefisch (BGR), Dr Yan Jia (ZAMG), Kristian Csicsay (ESISAS), MSc. Ines Ivančić (CEC). The majority of figures shown in the manuscript are built with the Generic Mapping Tools (GMT) library (Wessel & Smith 1998).

The authors are grateful to all their co-team members within the AlpArray Seismic Network Team (AASNT): György Hetényi, Rafael Abreu, Ivo Allegretti, Maria-Theresia Apoloner, Coralie Aubert, Simon Besançon, Maxime Bès de Berc, Didier Brunel, Marco Capello, Martina Čarman, Adriano Cavaliere, Jérôme Chèze, Claudio Chiarabba, Glenn Cougoulat, Luigia Cristiano, Tibor Czifra, Ezio D'Alema, Stefania Danesi, Romuald Daniel, Anke Dannowski, Iva Dasović, Anne Deschamps, Sven Egdorf, ETHZ-SED Electronics Lab, Tomislav Fiket, Kasper Fischer, Sigward Funke, Aladino Govoni, Gidera Gröschl, Stefan Heimers, Ben Heit, Davorka Herak, Johann Huber, Dejan Jarić, Petr Jedlička, Hélène Jund, Stefan Klingen, Bernhard Klotz, Petr Kolínský, Josef Kotek, Lothar Kühne, Krešo Kuk, Dietrich Lange, Jürgen Loos, Sara Lovati, Deny Malengros, Christophe Maron, Xavier Martin, Marco Massa, Francesco Mazzarini, Laurent Métral, Milena Moretti, Helena Munzarová, Anna Nardi, Jurij Pahor, Catherine Péquegnat, Florian Petersen, Davide Piccinini, Silvia Pondrelli, Snježan Prevolnik, Roman Racine, Marc Régnier, Miriam Reiss, Simone Salimbeni, Marco Santulin, Werner Scherer, Sven Schippkus, Detlef Schulte-Kortnack, Stefano Solarino, Kathrin Spieker, Josip Stipčević, Angelo Strollo, Bálint Süle, Gyöngyvér Szanyi, Eszter Szűcs, Martin Thorwart, Stefan Ueding, Massimiliano Vallocchia, Luděk Vecsey, René Voigt, Christian Weidle, Gauthier Weyland, Stefan Wiemer, Felix Wolf, David Wolyniec, Thomas Zieke.

DATA AVAILABILITY

The AARSC, the minimum 1-D model and station delays for the GAR are stored in a permanent data repository available here: https://doi.org/10.3929/ethz-b-000542191. We release the catalogue in different formats (csv, txt, QuakeML, SC3-XML). The minimum 1-D *P*-wave velocity model and the associated station delays are already in suitable format for the VELEST software. We also provide a dictionary for linking the station aliases to the corresponding inventory.

The ADAPT framework and all the individual pickers used in this study can be found at the first author's GitHub repository (https://github.com/mbagagli). Request for the VELEST software could be as well redirected to 'kiss@tomo.ig.erdw.ethz.ch'. We refer to the AlpArray project website (http://www.alparray.ethz.ch) for any data-related issues, while for any other questions please contact the corresponding authors. Researchers interested in the complete automatic seismic processing workflow are welcomed to contact the authors for any scientific project collaboration.

Waveform data from AASN stations and all other stations collected are available through EIDA (http://www.orfeus-eu.org/eida/). Visit http://www.alparray.ethz.ch/seismic_network/backbone/data-access for further information on data access and http://www.alparray.ethz.ch/seismic network/backbone/data-policy-and-citation for information of data policy. General information about the AlpArray project is available at www.alparray.ethz.ch. The temporary BB stations installed in AASN are under the Z3 network code (AlpArray Seismic Network, 2015). The station from the temporary AlpArray experiment CASE are available under the network code 8X (Molinari *et al*. 2019, AlpArray Seismic Network, 2016) The permanent stations are contributed via the following networks codes: AC (Institute of Geosciences, Energy, Water and Environment, 2002), BE (Royal Observatory Of Belgium, 1985), BW (Department of Earth And Environmental Sciences, Geophysical Observatory, University Of Munchen, 2001), CA (Institut Cartogràfic I Geològic De Catalunya, 1984), CH (Swiss Seismological Service (SED) at ETH Zurich, 1983), CR (University of Zagreb, 2001), CZ (Institute of Geophysics, Academy of Sciences of the Czech Republic, 1973), ES (Instituto Geografico Nacional, Spain, 1999), FR (RESIF, 1995a), G (Institut De Physique Du Globe De Paris (IPGP), & Ecole Et Observatoire Des Sciences De La Terre de Strasbourg (EOST), 1982), GE (GEOFON Data Centre, 1993), GR (Federal Institute for Geosciences and Natural Resources, 1976), GU (University of Genoa, 1967), HU (Ko¨vesligethy Rado´ Seismological Observatory, 1992), IU (Albuquerque Seismological Laboratory (ASL)/USGS, 1988), IV (INGV Seismological Data Centre, 2006), ME, MN (MedNet project partner institutions, 1990), MT (French Landslide Observatory–Seismological Datacenter / RESIF, 2006), NI (OGS (Istituto Nazionale di Oceanografia e di Geofisica Sperimentale) and University of Trieste, 2002), OE (ZAMG-Zentralanstalt Für Meterologie Und Geodynamik,1987), OX (OGS (Istituto Nazionale di Oceanografia e di Geofisica Sperimentale, 2016), PL, RA (RESIF, 1995b), RD (RESIF, 2018), RF (University of Trieste, 1993), SI, SJ, SK (ESISAS (Earth Science Institute of the

Downloaded from https://academic.oup.com/gji/article/231/2/921/6609778 by OGS (Istituto Nazionale di Oceanografia e di Geofisica Sperimentale-OGS) Borgo Grotta user on 11 December 2023

Slovak Academy of Sciences), 2004; Csicsay *et al*. 2018), SL (Slovenian Environment Agency, 2001), ST (Geological Survey-Provincia Autonoma di Trento, 1981), SX (Leipzig University, 2001), TH (Jena, F. S. U., 2009).

The regional earthquake bulletin of EPOS-EMSC from 1998 January 01 to 2019 December 31 was downloaded through the web-services offered at https://www.seismicportal.eu/fdsn-wsevent.html (last accessed 2022 January 27). The national earthquake bulletins collected from 2016 January 01 to 2019 December 31 of INGV (last accessed 2021 January 27), RESIF (last accessed 2021 January 27) and SED (last accessed 2021 January14) were downloaded with the FDSN web-service in their respective EIDA-nodes. The national earthquake bulletin of ASCR was downloaded from https://seisdb.ig.cas.cz/bull.html (last accessed 2021 July 15). The revised regional earthquake bulletin of OGS was downloaded from https://rts.crs.inogs.it (last accessed 2021 July 15). The revised national earthquake bulletin of KRSZO was extracted from the Hungarian National Seismological Bulletin (http://www.seismology.hu/index.php/en/seismicity/earthquake-bulletins/31-hungarian-national-seismological-bulletin) last accessed 2021-07-20. The national catalogue of ARSO, ESISAS, CEC, BGR and ZAMG were retrieved by personal communications.

Author Contribution Statement

E. Kissling and D. Giardini designed and supervised the project. M. Bagagli and E. Kissling designed the method. M. Bagagli developed the computational framework. I. Molinari collected and prepared the waveform and station meta data. T. Diehl and I. Molinari provided the conceptualization, technical implementation and application of the SeisComP3 detection procedure. M. Bagagli, I. Molinari, T. Diehl, E. Kissling, and D. Giardini analysed the data. M. Bagagli, I. Molinari and E. Kissling wrote the manuscript with additional contributions and support from the other co-authors.

Conflict of Interest:

The authors declare no conflicts of interest with respect to the research, authorship, and publicon of this article.

REFERENCES

Albuquerque Seismological Laboratory (ASL)/USGS, 1988. Global Seismograph Network (GSN - IRIS/USGS), International Federation of Digital Seismograph Networks, doi:10.7914/SN/IU

Aldersons, F. 2004. *Toward Three-dimensional Crustal Structure of the Dead Sea Region from Local Earthquake Tomography*, Citeseer.

AlpArray Seismic Network, 2015. AlpArray Seismic Network (AASN) temporary component, AlpArray Working Group, doi:10.12686/ALPARRAY/Z3_2015

AlpArray Seismic Network, 2016. Central Adriatic Seismic Experiment (CASE)—AlpArray; AlpArray Working Group. Other/Seismic Network.

Amorese, D. 2007. Applying a change-point detection method on frequency-magnitude distributions, *Bull. seism. Soc. Am.*, **97,** 1742–1749, Seismological Society of America.

Baer, M. & Kradolfer, U., 1987. An automatic phase picker for local and teleseismic events, *Bull. seism. Soc. Am.*, **77,** 1437–1445.

Bagagli, M. 2019. filterpicker-python, Zenodo, doi:10.5281/zenodo.3609025.

Bagagli, M. 2021a. aurempickers, Zenodo, doi:10.5281/zenodo.5459631.

Bagagli, M. 2021b. host-picker,Zenodo, https://doi.org/10.5281/zenodo.5575913.

Bagagli, M. 2022. *Seismicity and seismic tomography across scales: application to the greater Alpine region*, PhD thesis, ETH-Zürich.

Bagagli, M., Kissling, E., Piccinini, D. & Saccorotti, G., 2020. Local earthquake tomography of the Larderello-Travale geothermal field, *Geothermics,* **83,** 101731, doi:10.1016/j.geothermics.2019.101731

Baillard, C., Crawford, W.C., Ballu, V., Hibert, C. & Mangeney, A., 2014. An automatic kurtosis-based P- and S-phase picker designed for local seismic networks, *Bull. seism. Soc. Am.*, **104,** 394–409, GeoScienceWorld.

Bartel, E.M., Neubauer, F., Genser, J. & Heberer, B., 2014a. States of paleostress north and south of the Periadriatic fault: comparison of the Drau Range and the Friuli Southalpine wedge, *Tectonophysics,* **637,** 305–327.

Bartel, E.M., Neubauer, F., Heberer, B. & Genser, J., 2014b. A low-temperature ductile shear zone: the gypsum-dominated western extension of the brittle Fella-Sava Fault, Southern Alps, *J. Struct. Geol.,* **69,** 18–31.

Bethmann, F., Deichmann, N. & Mai, P.M., 2011. Scaling relations of local magnitude versus moment magnitude for sequences of similar earthquakes in Switzerland, *Bull. seism. Soc. Am.*, **101,** 515–534, Seismological Society of America.

Bindi, D., Zaccarelli, R., Strollo, A. & Di Giacomo, D., 2019. Harmonized local magnitude attenuation function for Europe using the European Integrated Data Archive (EIDA), *Geophys. J. Int.*, **218,** 519–533, Oxford University Press.

Blundell, D.J., Freeman, R., Mueller, S. & Button, S., 1992. *A Continent Revealed: The European Geotraverse, Structure and Dynamic Evolution*, Cambridge University Press.

Braclawska, A. & Idziak, A.F., 2019. Unification of data from various seismic catalogues to study seismic activity in the Carpathians Mountain arc, *Open Geosci.*, **11,** 837–842, De Gruyter.

Bratt, S.R. & Nagy, W., 1991. The LocSAT Program, *Science Applications International Corporation*, San Diego.

Brückl, E., Behm, M., Decker, K., Grad, M., Guterch, A., Keller, G.R. & Thybo, H., 2010. Crustal structure and active tectonics in the Eastern Alps, *Tectonics,* 29, doi:10.1029/2009TC002491.

Cao, A. & Gao, S.S., 2002. Temporal variation of seismic b-values beneath northeastern Japan island arc, *Geophys. Res. Lett.*, **29,** 48–1, Wiley Online Library.

Carminati, E. & Doglioni, C.(2012) Alps vs. Apennines: the paradigm of a tectonically asymmetric Earth. *Earth-Sci. Rev.,* **112,** 67–96.

Castellarin, A., Vai, G.B. & Cantelli, L., 2006. The Alpine evolution of the Southern Alps around the Giudicarie faults: a Late Cretaceous to Early Eocene transfer zone, *Tectonophysics TRANSALP,* **414,** 203–223.

Chiarabba, C., Giacomuzzi, G., Bianchi, I., Agostinetti, N.P. & Park, J., 2014. From underplating to delamination-retreat in the northern Apennines, *Earth planet. Sci. Lett.,* **403,** 108–116.

Chorowicz, J., 1970. La transversale de Zrmanja (Yougoslavie), *Bull. Soc. Géol. France,* **7,** 1028–1033, Societe Geologique de France Paris, France.

Cichowicz, A., 1993. An automatic S-phase picker, *Bull. seism. Soc. Am.*, **83,** 180–189.

Collettini, C. & Barchi, M.R., 2002. A low-angle normal fault in the Umbria region (Central Italy): a mechanical model for the related microseismicity, *Tectonophysics,* **359,** 97–115.

Cooley, J.W. & Tukey, J.W., 1965. An algorithm for the machine calculation of complex Fourier Series, *Math. Comput.*, **19,** 297–301, American Mathematical Society.

Csicsay, K. *et al.*, 2018. The National Network of Seismic Stations of Slovakia–Current state after 13 years in operation from the project of modernization and enhancement, *Contrib. Geophys. Geod.,* **48,** 337–348.

Csontos, L. & Nagymarosy, A., 1998. The Mid-Hungarian line: a zone of repeated tectonic inversions, *Tectonophysics,* **297,** 51–71.

D'Acquisto, M., Dal Zilio, L., Molinari, I., Kissling, E., Gerya, T. & Dinther, Y. van., 2020. Tectonics and seismicity in the Northern Apennines driven by slab retreat and lithospheric delamination, *Tectonophysics,* **789,** 228481, doi:10.1016/j.tecto.2020.228481

Deichmann, N. 1992. Structural and rheological implications of lower-crustal earthquakes below northern Switzerland, *Phys. Earth planet. Inter.*, **69,** 270–280, Elsevier.

Downloaded from https://academic.oup.com/gji/article/231/2/921/6609778 by OGS (Istituto Nazionale di Oceanografia e di Geofisica Sperimentale-OGS) Borgo Grotta user on 11 December 2023

Deichmann, N., 2017. Theoretical basis for the observed break in ML/M w scaling between small and large earthquakes, *Bull. seism. Soc. Am.*, **107,** 505–520, Seismological Society of America.

Delacou, B., Sue, C., Champagnac, J.-D. & Burkhard, M., 2004. Present-day geodynamics in the bend of the western and central Alps as constrained by earthquake analysis, *Geophys. J. Int.*, **158,** 753–774, Blackwell Publishing Ltd Oxford, UK.

Department Of Earth And Environmental Sciences, Geophysical Observatory, University Of Munchen, 2001. BayernNetz, International Federation of Digital Seismograph Networks, doi:10.7914/SN/BW

Diehl, T., Deichmann, N., Kissling, E. & Husen, S., 2009b. Automatic S-Wave Picker for Local Earthquake Tomography, *Bull. seism. Soc. Am.*, **99,** 1906–1920.

Diehl, T., Husen, S., Kissling, E. & Deichmann, N., 2009c. High-resolution 3-D P-wave model of the Alpine crust, *Geophys. J. Int.*, **179,** 1133–1147, Oxford Academic.

Diehl, T., Kissling, E., Husen, S. & Aldersons, F., 2009a. Consistent phase picking for regional tomography models: application to the greater Alpine region, *Geophys. J. Int.*, **176,** 542–554.

Diehl, T., Singer, J., Hetényi, G., Grujic, D., Clinton, J., Giardini, D. & Kissling, E., 2017. Seismotectonics of Bhutan: Evidence for segmentation of the Eastern Himalayas and link to foreland deformation, *Earth planet. Sci. Lett.*, **471,** 54–64.

Eva, E., Malusà, M.G. & Solarino, S., 2020. Seismotectonics at the transition between opposite-dipping slabs (western Alpine region), *Tectonics*, **39,** Wiley Online Library, doi.org/10.1029/2020TC006086.

Eva, E. & Solarino, S., 1998. Variations of stress directions in the western Alpine arc, *Geophys. J. Int.*, **135,** 438–448, Blackwell Science Ltd Oxford, UK.

Federal Institute for Geosciences and Natural Resources, 1976. German Regional Seismic Network (GRSN), Bundesanstalt für Geowissenschaften und Rohstoffe, doi:10.25928/MBX6-HR74

Font, Y., Kao, H., Lallemand, S., Liu, C.-S. & Chiao, L.-Y., 2004. Hypocentre determination offshore of eastern Taiwan using the Maximum Intersection method, *Geophys. J. Int.*, **158,** 655–675.

French Landslide Observatory–Seismological Datacenter /RESIF, 2006. Observatoire Multi-disciplinaire des Instabilités de Versants (OMIV), RESIF-Réseau Sismologique et géodésique Français, doi:10.15778/RESIF.MT

Frepoli, A. & Amato, A., 1997. Contemporaneous extension and compression in the Northern Apennines from earthquake fault-plane solutions, *Geophys. J. Int.*, **129,** 368–388.

Frost, E., Dolan, J., Sammis, C., Hacker, B., Cole, J. & Ratschbacher, L., 2009. Progressive strain localization in a major strike-slip fault exhumed from midseismogenic depths: structural observations from the Salzach-Ennstal-Mariazell-Puchberg fault system, Austria, *J. geophys. Res.: Solid Earth*, **114,** Wiley Online Library, doi.org/10.1029/2008JB005763.

Fuchs, F., Kolínský, P., Gröschl, G. & Bokelmann, G., the AlpArray Working Group, 2016. AlpArray in Austria and Slovakia: technical realization, site description and noise characterization, *Adv. Geosci.*, **43,** 1–13- EGU General Assembly 2016, Vienna, Austria.

GEOFON Data Centre, 1993. GEOFON Seismic Network, *Deutsches GeoForschungsZentrum GFZ*, doi:10.14470/TR560404

Giardini, D. *et al.*, 2018. Seismic hazard map of the Middle East, *Bull. Earthq. Eng.*, **16,** 3567–3570.

Giardini, D., Grünthal, G., Shedlock, K.M. & Zhang, P., 1999. The GSHAP global seismic hazard map, *Ann. Geophys.*, 42, http://hdl.handle.net/2122/1396.

Goertz-Allmann, B.P., Edwards, B., Bethmann, F., Deichmann, N., Clinton, J., Fäh, D. & Giardini, D., 2011. A new empirical magnitude scaling relation for Switzerland, *Bull. seism. Soc. Am.*, **101,** 3088–3095, Seismological Society of America.

Govoni, A. *et al.*, 2017. AlpArray-Italy: site description and noise characterization. *Adv. Geosci.*, **43,** 39–52, EGU General Assembly 2016, Vienna, Austria, Copernicus GmbH.

Gráczer, Z. *et al.*, 2018. AlpArray in Hungary: temporary and permanent seismological networks in the transition zone between the Eastern Alps and the Pannonian basin, *Acta Geod. Geophys.*, **53,** 221–245.

Grützner, C. *et al.*, 2021. Holocene surface-rupturing earthquakes on the Dinaric Fault System, western Slovenia, *Solid Earth*, **12,** 2211–2234, Copernicus GmbH.

Handy, M.R., Schmid, S.M., Bousquet, R., Kissling, E. & Bernoulli, D, 2010. Reconciling plate-tectonic reconstructions of Alpine Tethys with the geological–geophysical record of spreading and subduction in the Alps, *Earth-Sci. Rev.*, **102,** 121–158.

Handy, M.R., Ustaszewski, K. & Kissling, E., 2015. Reconstructing the Alps–Carpathians–Dinarides as a key to understanding switches in subduction polarity, slab gaps and surface motion, *Int. J. Earth Sci. (Geol Rundsch)*, **104,** 1–26.

Hanka, W., Saul, J., Weber, B., Becker, J. & Harjadi, P., Seismology Group GITEWS, 2010. Real-time earthquake monitoring for tsunami warning in the Indian Ocean and beyond, *Natural Hazards Earth Syst. Sci.*, **10,** 2611–2622, Copernicus GmbH.

Haslinger, F. *et al.*, 1999. 3D crustal structure from local earthquake tomography around the Gulf of Arta (Ionian region, NW Greece), *Tectonophysics*, **304,** 201–218.

Herrmann, M. & Marzocchi, W., 2020. Inconsistencies and lurking pitfalls in the magnitude–frequency distribution of high-resolution earthquake catalogs, *Seismol. Res. Lett.*, **92,** 909–922.

Hetényi, G. *et al.*, 2018. The AlpArray Seismic Network: a large-scale European experiment to image the Alpine Orogen, *Surv. Geophys.*, **39,** 1009–1033.

Horváth, F. & Cloetingh, S., 1996. Stress-induced late-stage subsidence anomalies in the Pannonian basin, *Tectonophysics*, **266,** 287–300.

Husen, S., Kissling, E. & Clinton, J.F., 2011. Local and regional minimum 1D models for earthquake location and data quality assessment in complex tectonic regions: application to Switzerland, *Swiss J. Geosci*., **104,** 455–469.

Husen, S., Kissling, E., Flueh, E. & Asch, G., 1999. Accurate hypocentre determination in the seismogenic zone of the subducting Nazca Plate in northern Chile using a combined on-/offshore network, *Geophys. J. Int.*, **138,** 687–701, Blackwell Publishing Ltd Oxford, UK.

INGV Seismological Data Centre, 2006. Rete Sismica Nazionale (RSN), *Istituto Nazionale di Geofisica e Vulcanologia (INGV)*, Italy, doi:10.18715/GEOSCOPE.G

Institut Cartogràfic I Geològic De Catalunya, 1984. Catalan Seismic Network, International Federation of Digital Seismograph Networks, doi:10.18715/GEOSCOPE.G

Institut De Physique Du Globe De Paris (IPGP) & Ecole Et Observatoire Des Sciences De La Terre De Strasbourg (EOST), 1982. *GEOSCOPE, French Global Network of broad band seismic stations*, Institut de physique du globe de Paris (IPGP), Université de Paris, doi:10.18715/GEOSCOPE.G

Institute Of Geophysics, Academy of Sciences of the Czech Republic, 1973. Czech Regional Seismic Network, International Federation of Digital Seismograph Networks, doi:10.7914/SN/CZ

Institute Of Geosciences, Energy, Water and Environment, 2002. Albanian Seismological Network, International Federation of Digital Seismograph Networks, doi:10.7914/SN/AC

Instituto Geografico Nacional, Spain, 1999. Spanish Digital Seismic Network, International Federation of Digital Seismograph Networks, doi:10.7914/SN/ES

Jena, Friedrich-Schiller-University (F. S. U.), 2009. Thüringer Seismologisches Netz (TSN), International Federation of Digital Seismograph Networks, doi:10.7914/SN/TH

Johnson, C.E., Bittenbinder, A., Bogaert, B., Dietz, L. & Kohler, W., 1995. Earthworm: a flexible approach to seismic network processing, *Iris Newslett.*, **14,** 1–4.

Jozi Najafabadi, A. *et al.*, 2021. Relocation of earthquakes in the southern and eastern Alps (Austria, Italy) recorded by the dense, temporary SWATH-D network using a Markov chain Monte Carlo inversion, *Solid Earth*, **12,** 1087–1109, Copernicus GmbH.

Kästle, E.D., Rosenberg, C., Boschi, L., Bellahsen, N., Meier, T. & El-Sharkawy, A., 2020. Slab break-offs in the Alpine subduction zone, *Int. J. Earth Sci. (Geol Rundsch)*, **109,** 587–603.

Kennet, B.L.N. 1991. Iaspei 1991 seismological tables. *Terra Nova*, **3,** 122–122. doi:

Downloaded from https://academic.oup.com/gji/article/231/2/921/6609778 by OGS (Istituto Nazionale di Oceanografia e di Geofisica Sperimentale-OGS) Borgo Grotta user on 11 December 2023

Kissling, E. 1988. Geotomography with local earthquake data, *Rev. Geophys.,* **26,** 659–698.
Kissling, E., Ellsworth, W.L., Eberhart-Phillips, D. & Kradolfer, U., 1994. Initial reference models in local earthquake tomography, *J. geophys. Res.: Solid Earth,* **99,** 19635–19646.
Kissling, E., Kradolfer, U. & Maurer, H., 1995. Program VELEST user's guide-Short Introduction. Retrieved from Institute of Geophysics, ETH Zurich.
Kissling, E. & Schlunegger, F., 2018. Rollback orogeny model for the evolution of the Swiss Alps, *Tectonics,* **37,** 1097–1115.
Kissling, E., Schmid, S.M., Lippitsch, R., Ansorge, J. & Fügenschuh, B., 2006. Lithosphere structure and tectonic evolution of the Alpine arc: new evidence from high-resolution teleseismic tomography, *Geol. Soc. Lond. Mem.,* **32,** 129–145, Geological Society of London.
Kövesligethy Radó Seismological Observatory, 1992. Hungarian National Seismological Network. Deutsches GeoForschungsZentrum GFZ, doi:10.14470/UH028726.
Krischer, L., Megies, T., Barsch, R., Beyreuther, M., Lecocq, T., Caudron, C. & Wassermann, J., 2015. ObsPy: a bridge for seismology into the scientific Python ecosystem, *Comput. Sci. Discov.,* **8,** 014003, IOP Publishing, doi:10.1088/1749-4699/8/1/014003
Küperkoch, L., Meier, T., Lee, J. & Friederich, W., Working Group E., 2010. Automated determination of P -phase arrival times at regional and local distances using higher order statistics, *Geophys. J. Int.,* doi:10.1111/j.1365-246X.2010.04570.x
Lardeaux, J.-M., Schwartz, S., Tricart, P., Paul, A., Guillot, S., Béthoux, N. & Masson, F., 2006. A crustal-scale cross-section of the south-western Alps combining geophysical and geological imagery, *Terra Nova,* **18,** 412–422, Wiley Online Library.
Laubscher, H.P. 1971. Das Alpen-Dinariden-Problem und die Palinspastik der südlichen Tethys, *Geol. Rundsch.,* **60,** 813–833. doi:10.1007/BF02046522
Leipzig University, 2001. SXNET Saxon Seismic Network, International Federation of Digital Seismograph Networks. doi:10.7914/SN/SX
Lenhardt, W.A., Švancara, J., Melichar, P., Pazdírková, J., Havíř, J. & Sýkorová, Z., 2007. Seismic activity of the Alpine-Carpathian-Bohemian Massif region with regard to geological and potential field data, *Geologica Carpathica,* **58,4,**397–412.
Lilliefors, H.W. 1967. On the Kolmogorov-Smirnov test for normality with mean and variance unknown, *J. Am. Stat. Assoc.,* **62,** 399–402, Taylor & Francis.
Lolli, B., Gasperini, P., Mele, F.M. & Vannucci, G., 2015. Recalibration of the distance correction term for local magnitude (ML) computations in Italy, *Seismol. Res. Lett.,* **86,** 1383–1392, Seismological Society of America.
Lomax, A., Satriano, C. & Vassallo, M., 2012. Automatic picker developments and optimization: FilterPicker—a robust, broadband picker for real-time seismic monitoring and earthquake early warning, *Seismol. Res. Lett.,* **83,** 531–540.
Lomax, A., Virieux, J., Volant, P. & Berge-Thierry, C., 2000. Probabilistic earthquake location in 3D and layered models, in *Advances in Seismic Event Location Modern Approaches in Geophysics*eds. C.H., Thurber & N., Rabinowitz 101–134, Dordrecht, Springer Netherlands.
Mader, S. & Ritter, J.R.R., 2021. The StressTransfer seismic network—an experiment to monitor seismically active fault zones in the Northern Alpine Foreland of Southwestern Germany, *Seismol. Res. Lett.,* **92,** 1773–1787.
Maeda, N.(1985) A method for reading and checking phase times in autoprocessing system of seismic wave data. *Zisin,* **38,** 365–379.
Malusà, M.G. *et al.*, 2021. The deep structure of the Alps based on the CIFALPS seismic experiment: a synthesis, *Geochem. Geophys. Geosyst.,* **22,** Wiley Online Library, doi.org/10.1029/2020GC009466.
Marzocchi, W. & Sandri, L., 2003. A review and new insights on the estimation of the b-value and its uncertainty, *Ann. Geophys.,* **46,** http://hdl.handle.net/2122/1017.
Mathey, M. *et al.*, 2021. Present-day geodynamics of the Western Alps: new insights from earthquake mechanisms, *Solid Earth,* **12,** 1661–1681, Copernicus GmbH.
Maurer, V., Kissling, E., Husen, S. & Quintero, R., 2010. Detection of systematic errors in travel-time data using a minimum 1D model: application to Costa Rica seismic tomography, *Bull. seism. Soc. Am.,* **100,** 629–639.
McNamara, D.E. & Buland, R.P., 2004. Ambient noise levels in the continental United States, *Bull. seism. Soc. Am.,* **94,** 1517–1527.
MedNet Project Partner Institutions, 1990. Mediterranean Very Broadband Seismographic Network (MedNet), Istituto Nazionale di Geofisica e Vulcanologia (INGV). https://doi.org/10.13127/SD/FBBBTDTD6Q
Mignan, A. 2012. Functional shape of the earthquake frequency-magnitude distribution and completeness magnitude, *J. geophys. Res.: Solid Earth,* **117,** Wiley Online Library, doi.org/10.1029/2012JB009347.
Mignan, A. & Woessner, J., 2012. Estimating the magnitude of completeness for earthquake catalogs, Community Online Resource for Statistical Seismicity Analysis, doi.org/10.5078/corssa-00180805.
Molinari, I. *et al.*, 2016. Swiss-AlpArray temporary broadband seismic stations deployment and noise characterization, *Adv. Geosci.*,**43,** 15–29, Copernicus GmbH.
Molinari, I. *et al.*, 2019. Investigation of the Central Adriatic lithosphere structure with the AlpArray-CASE seismic experiment, *Geofizika,* **35,** 103–128.
Molli, G., Crispini, L., Malusà, M.G., Mosca, P., Piana, F. & Federico, L., 2010. Geology of the Western Alps-Northern Apennine junction area: a regional review, *J. Virt. Ex.,* 36, doi:10.7914/SN/OX
Mueller, C.S. 2019. Earthquake catalogs for the USGS national seismic hazard maps, *Seismol. Res. Lett.,* **90,** 251–261, Seismological Society of America.
Munafò, I., Malagnini, L. & Chiaraluce, L., 2016. On the relationship between M w and ML for small earthquakes, *Bull. seism. Soc. Am.,* **106,** 2402–2408, Seismological Society of America.
OGS (Istituto Nazionale Di Oceanografia E Di Geofisica Sperimentale) And University Of Trieste, 2002. North-East Italy Broadband Network, International Federation of Digital Seismograph Networks. doi:10.7914/SN/NI
OGS (Istituto Nazionale Di Oceanografia E Di Geofisica Sperimentale), 2016. North-East Italy Seismic Network, International Federation of Digital Seismograph Networks. doi:10.7914/SN/OX
Pamić, J., Gušić, I. & Jelaska, V., 1998. Geodynamic evolution of the Central Dinarides, *Tectonophysics,* **297,** 251–268.
Pearson, E.S. & Hartley, H.O., 1972. *Biometrika Tables for Statisticians: Vol II,* Cambridge (Eng.), University Press.
Petersen, G.M., Cesca, S. & Kriegerowski, M., the AlpArray Working Group, 2019. Automated quality control for large seismic networks: implementation and application to the AlpArray Seismic Network, *Seismol. Res. Lett.,* **90,** 1177–1190.
Pistone, M., Ziberna, L., Hetényi, G., Scarponi, M., Zanetti, A. & Müntener, O., 2020. Joint geophysical-petrological modeling on the Ivrea geophysical body beneath Valsesia, Italy: constraints on the continental lower crust, *Geochem. Geophys. Geosyst.,* **21,** Wiley Online Library, doi.org/10.1029/2020GC009397.
Poljak, M., Živčić, M. & Zupančič, P., 2000. The seismotectonic characteristics of Slovenia, *Pure appl. geophys,* **157,** 37–55.
Pope, A.J. 1976. *The Statistics of Residuals and the Detection of Outliers,* US Department of Commerce, National Oceanic and Atmospheric Administration.
Pujol, J. 1988. Comments on the joint determination of hypocenters and station corrections, *Bull. seism. Soc. Am.,* **78,** 1179–1189.
Pujol, J. 2000. Joint event location—the JHD technique and applications to data from local seismic networks, in *Advances in Seismic Event Location Modern Approaches in Geophysics*eds. C.H., Thurber & N., Rabinowitz, 163–204, Dordrecht, Springer Netherlands.
Quintero, R. & Kissling, E., 2001. An improved P-wave velocity reference model for Costa Rica, *Geofís. Int.,* **40,** 3–19, Universidad Nacional Autónoma de México.
Ratschbacher, L., Merle, O., Davy, P. & Cobbold, P., 1991. Lateral extrusion in the eastern Alps, Part 1: boundary conditions and experiments scaled for gravity, *Tectonics,* **10,** 245–256.
Reiter, F., Freudenthaler, C., Hausmann, H., Ortner, H., Lenhardt, W. & Brandner, R., 2018. Active seismotectonic deformation in front of the Dolomites Indenter, Eastern Alps, *Tectonics,* **37,** 4625–4654.

Downloaded from https://academic.oup.com/gji/article/231/2/921/6609778 by OGS (Istituto Nazionale di Oceanografia e di Geofisica Sperimentale-OGS) Borgo Grotta user on 11 December 2023

Reiter, F., Ortner, H. & Brandner, R., 2003. Seismically active Inntal fault zone: inverted European rift structures control upper plate deformation, *Mem. Sci. Geol*, **54,** 233–234.

RESIF. 1995. RESIF-RLBP French Broad-band network, RESIF-RAP strong motion network and other seismic stations in metropolitan France, RESIF—Réseau Sismologique et géodésique Français. doi:10.15778/RESIF.FR

RESIF. 1995. RESIF-RAP French Accelerometric Network, RESIF—Réseau Sismologique et géodésique Français. doi:10.15778/RESIF.RA

RESIF. 2018. CEA/DASE broad-band permanent network in metropolitan France, RESIF—Réseau Sismologique et géodésique Français. doi:10.15778/RESIF.RD

Rezaeifar, M. & Kissling, E., 2018. Compilation of a high-quality catalogue for M3. 0+ seismicity in northern Iran region for the period of 2005–2017, *Geophys. J. Int.*, **215,** 118–132, Oxford University Press.

Richter, C.F. 1935. An instrumental earthquake magnitude scale, *Bull. seism. Soc. Am.*, **25,** 1–32, The Seismological Society of America.

Rojo Limón, G., Kissling, E., Ouillon, G. & Sornette, D., 2021. A consistent and high-quality M4+ earthquake catalogue for Turkey 2007–2016 from two independent catalogues, *Geophys. J. Int.*, **225,** 711–728, Oxford University Press.

Rosenberg, C.L. & Schneider, S., 2008. The western termination of the SEMP Fault (eastern Alps) and its bearing on the exhumation of the Tauern Window, *Geol. Soc. Lond. Spec. Publ.*, **298,** 197–218, Geological Society of London.

Rosenberg, C.L., Schneider, S., Scharf, A., Bertrand, A., Hammerschmidt, K., Rabaute, A. & Brun, J.-P., 2018. Relating collisional kinematics to exhumation processes in the Eastern Alps. *Earth-Sci. Rev.*, **176,** 311–344.

Rovida, A.N., Locati, M., CAMASSI, R.D., Lolli, B. & Gasperini, P., 2016. CPTI15, the 2015 version of the Parametric Catalogue of Italian Earthquakes, Istituto Nazionale di Geofisica e Vulcanologia (INGV), http://doi.org/10.6092/INGV.IT-CPTI15.

Royal Observatory Of Belgium, 1985. Belgian Seismic Network, International Federation of Digital Seismograph Networks. doi:10.7914/SN/BE

Saragiotis, C.D., Hadjileontiadis, L.J. & Panas, S.M., 2002. PAI-S/K: a robust automatic seismic P phase arrival identification scheme, *IEEE Trans. Geosci. Remote Sens.*, **40,** 1395–1404, IEEE.

Sawires, R., Santoyo, M.A., Peláez, J.A. & Corona Fernández, R.D., 2019. An updated and unified earthquake catalog from 1787 to 2018 for seismic hazard assessment studies in Mexico, *Sci. data*, **6,** 1–14, Nature Publishing Group.

Scarponi, M., Hetényi, G., Plomerová, J., Solarino, S., Baron, L. & Petri, B., 2021. Joint seismic and gravity data inversion to image intra-crustal structures: the Ivrea Geophysical Body along the Val Sesia profile (Piedmont, Italy), *Front. Earth Sci.*, doi.org/10.3389/feart.2021.671412.

Schmid, S.M. *et al.*, 2008. The Alpine-Carpathian-Dinaridic orogenic system: correlation and evolution of tectonic units, *Swiss J. Geosci.*, **101,** 139–183, SpringerOpen.

Schmid, S.M., Fügenschuh, B., Kissling, E. & Schuster, R., 2004. Tectonic map and overall architecture of the Alpine orogen, *Eclog. Geol. Helvetiae*, **97,** 93–117, SpringerOpen.

Schmid, S.M., Kissling, E., Diehl, T., Hinsbergen, D.J. & Molli, G., 2017. Ivrea mantle wedge, arc of the Western Alps, and kinematic evolution of the Alps–Apennines orogenic system, *Swiss J. Geosci.*, **110,** 581–612, Springer.

Schorlemmer, D., Euchner, F., Kästli, P. & Saul, J., 2011. QuakeML: status of the XML-based seismological data exchange format, *Ann. Geophys.*, **54,** 59–65.

Scognamiglio, L. *et al.*, 2012. The 2012 Pianura Padana Emiliana seimic sequence: locations, moment tensors and magnitudes, *Ann. Geophys.*, 55, http://hdl.handle.net/2122/11550.

Shi, Y. & Bolt, B.A., 1982. The standard error of the magnitude-frequency b value, *Bulletin of the Seismological Society of America*, **72,** 1677–1687, The Seismological Society of America.

Singer, J., Diehl, T., Husen, S., Kissling, E. & Duretz, T., 2014. Alpine lithosphere slab rollback causing lower crustal seismicity in northern foreland, *Earth planet. Sci. Lett.*, **397,** 42–56.

Slovenian Environment Agency, 2001. Seismic Network of the Republic of Slovenia, International Federation of Digital Seismograph Networks. doi:10.7914/SN/SL

Sohn, B.Y. & Kim, G.B., 1997. Detection of outliers in weighted least squares regression, *Korean J. Comp. Appl. Math.*, **4,** 441–452.

Solarino, S. *et al.*, 1997. Compilation of a recent seismicity data base of the greater Alpine region from several seismological networks and preliminary 3D tomographic results, http://hdl.handle.net/2122/1542.

Spada, M., Bianchi, I., Kissling, E., Agostinetti, N.P. & Wiemer, S., 2013. Combining controlled-source seismology and receiver function information to derive 3-D Moho topography for Italy, *Geophys. J. Int.*, **194,** 1050–1068, Oxford University Press.

Staudenmaier, N., Tormann, T., Edwards, B., Mignan, A. & Wiemer, S., 2019. The frequency-size scaling of non-volcanic tremors beneath the San Andreas Fault at Parkfield: possible implications for seismic energy release, *Earth planet. Sci. Lett.*, **516,** 77–107.

Stephens, M.A. 1974. EDF statistics for goodness of fit and some comparisons, *J. Am. Stat. Assoc.*, **69,** 730–737, Taylor & Francis.

Sue, C., Delacou, B., Champagnac, J.-D., Allanic, C., Tricart, P. & Burkhard, M., 2007. Extensional neotectonics around the bend of the Western/Central Alps: an overview, *Int. J. Earth Sci. (Geol Rundsch)*, **96,** 1101–1129.

Swiss Seismological Service (SED) At ETH Zurich 1983. National Seismic Networks of Switzerland, ETH Zürich.

Tinti, S. & Mulargia, F., 1987. Confidence intervals of b values for grouped magnitudes, *Bull. seism. Soc. Am.*, **77,** 2125–2134, The Seismological Society of America.

University Of Genoa 1967. Regional Seismic Network of North Western Italy, International Federation of Digital Seismograph Networks.doi:10.7914/SN/GU

University Of Zagreb 2001. Croatian Seismograph Network, International Federation of Digital Seismograph Networks. doi:10.7914/SN/CR

Ustaszewski, K., Schmid, S.M., Fügenschuh, B., Tischler, M., Kissling, E. & Spakman, W., 2008. A map-view restoration of the Alpine-Carpathian-Dinaridic system for the Early Miocene, *Swiss J. Geosci.*, **101,** 273–294, Springer.

van Ede, M.C., Molinari, I., Imperatori, W., Kissling, E., Baron, J. & Morelli, A., 2020. Hybrid broadband seismograms for seismic shaking scenarios: An application to the Po Plain sedimentary Basin (Northern Italy), *Pure appl. Geophys.*, **177,** 2181–2198, Springer.

Vecsey, L., Plomerová, J., Jedlička, P., Munzarová, H. & Babuška, V., the AlpArray working group, 2017. Data quality control and tools in passive seismic experiments exemplified on the Czech broadband seismic pool MOBNET in the AlpArray collaborative project, *Geosci. Instrum. Methods Data Syst.*, **6,** 505–521, Copernicus GmbH.

Verwater, V.F., Le Breton, E., Handy, M.R., Picotti, V., Jozi Najafabadi, A. & Haberland, C., 2021. Neogene kinematics of the Giudicarie Belt and eastern Southern Alpine orogenic front (northern Italy), *Solid Earth*, **12,** 1309–1334, Copernicus GmbH.

Wessel, P. & Smith, W.H.F., 1998. New, improved version of generic mapping tools released, *Eos, Trans. Am. geophys. Un.*, **79,** 579–579.

Wiemer, S. & Wyss, M., 2000. Minimum magnitude of completeness in earthquake catalogs: examples from Alaska, the western United States, and Japan, *Bull. seism. Soc. Am.*, **90,** 859–869, Seismological Society of America.

Woessner, J. *et al.*, 2015. The 2013 European Seismic Hazard Model: key components and results, *Bull. Earthq. Eng.*, **13,** 3553–3596.

Woessner, J. & Wiemer, S., 2005. Assessing the quality of earthquake catalogues: Estimating the magnitude of completeness and its uncertainty, *Bull. seism. Soc. Am.*, **95,** 684–698, Seismological Society of America.

Wyss, M., Hasegawa, A., Wiemer, S. & Umino, N., 1999. Quantitative mapping of precursory seismic quiescence before the 1989, M 7.1 off-Sanriku earthquake, Japan, *Ann. Geophys.*, **42,** doi.org/10.4401/ag-3765.

ZAMG-Zentralanstalt Für Meterologie Und Geodynamik, 1987. Austrian Seismic Network, International Federation of Digital Seismograph Networks. doi:10.7914/SN/OE

Downloaded from https://academic.oup.com/gji/article/231/2/921/6609778 by OGS (Istituto Nazionale di Oceanografia e di Geofisica Sperimentale-OGS) Borgo Grotta user on 11 December 2023